UNIVERSITÉ DU QUÉBEC À RIMOUSKI

LA PHOTORÉACTIVITÉ DE LA MATIÈRE ORGANIQUE DISSOUTE DANS LES EAUX SOUTERRAINES D'UNE ÎLE SUBARCTIQUE

(PHOTOREACTIVITY OF DISSOLVED ORGANIC MATTER IN GROUNDWATER OF A SUB-ARCTIC ISLAND)

MÉMOIRE

PRÉSENTÉ À

L'UNIVERSITÉ DU QUÉBEC À RIMOUSKI

comme exigence partielle

du programme de la maîtrise en océanographie

PAR

Liming Qi

Avril 2018

UNIVERSITÉ DU QUÉBEC À RIMOUSKI
Service de la bibliothèque

Avertissement

Acknowledgments

RÉSUMÉ

Les eaux souterraines sont des sources potentielles importantes de matière organique dissoute (DOM) pour les eaux côtières. Là, cette matière est soumise à des transformations photochimiques susceptibles d'influencer d'importants processus biogéochimiques marins. Par ailleurs, comme la DOM présente dans les aquifères est généralement peu ou pas exposée à la lumière, elle représente un substrat très intéressant pour étudier la photoréactivité de certaines matières organiques sources, ayant des caractéristiques particulières. Dans cette étude, réalisée sur un aquifère des Îles-de-la-Madeleine dans le Golfe St-Laurent, nous avons recueilli des échantillons DOM à deux stations situées le long d'un transect orienté de la plage vers l'intérieur des terres. Les échantillons ont été caractérisés par spectroscopies d'absorbance et de fluorescence et leur photoréactivité a été comparée. La DOM de l'eau souterraine de la plage (beach groundwater, BGW) était âgée, très colorée et d'origine terrigène. Elle avait un poids moléculaire élevé (MW), une forte humification et un faible contenu en protéines. La DOM de l'eau souterraine plus à l'intérieur des terres (inland groundwater, IGW) contenait du matériel frais, moins coloré et d'origine microbienne. Elle présentait un faible poids moléculaire (MW), un faible degré d'humification et un contenu en protéines élevé. Pour les deux échantillons, BGW et IGW, l'exposition à des radiations solaires simulées a entraîné une augmentation du rapport E_2/E_3, de l'indice biologique (BIX) et de la concentration en ammonium (NH_4^+) et une diminution d'absorbance, du coefficient d'absorption spécifique à 254 nm ($SUV\alpha_{254}$), de l'indice de fluorescence (FI), de l'indice d'humification (HIX), du MW et du carbone organique dissous (DOC). L'irradiation a également réduit les intensités des pics de fluorescence de type humique et des

III

composants humiques modélisés par le traitement statistique PARAFAC. En se basant sur la perte relative d'absorption, suite à l'irradiation, les changements photochimiquement induits dans BGW étaient comparables à ceux dans IGB pour SUVα_{254} et considérablement plus grands pour MW, BIX et DOC, et substantiellement plus petits pour FIX, HIX. Sur la base des photons absorbés, la DOM de BGW était beaucoup plus, modérément plus et moins photoréactive que la DOM de IGW en termes de photoblanchiment d'absorbance, de photominéralisation du DOC et de la photoammonification, respectivement. Les résultats de cette étude, en combinaison avec des travaux antérieurs pour les eaux de surface, conduisent à la formulation d'un paradigme provisoire: la DOM d'origine terrigène est plus sujet au photoblanchiment de l'absorbance, mais moins sujet à la photoammonification que la DOM d'origine microbienne, alors que les deux DOM présentent des réactivités comparables en ce qui concerne la photominéralisation du DOC. Le contenu scientifique de ce memoire a été publié dans Marine Chemistry avec la citation de : Qi L, Xie H, Gagné J-P, Chaillou G, Massicotte P, Yang G-P, 2018. Photoreactivities of two distinct dissolved organic matter pools in groundwater of a subarctic island. Marine Chemistry, https://doi.org/10.1016/j.marchem.2018.03.003.

Abstract

Groundwater is a potentially significant source of dissolved organic matter (DOM) to coastal oceans where it is subject to photochemical transformation and thus possibly influences major marine biogeochemical processes. Furthermore, groundwater DOM usually receives little prior light exposure, making it suitable for probing the photoreactivity of source organic materials. In this study we collected two DOM pools in beach and inland groundwater of the Îles-de-la-Madeleine in the Gulf of St. Lawrence, characterized them with absorbance and fluorescence spectroscopy, and compared their photoreactivities. Beach groundwater (BGW) primarily comprised old, highly colored terrestrial DOM having high molecular weight (MW), strong humification, and low protein contents, whereas inland groundwater (IGW) largely contained fresh, less colored microbial-derived DOM with low molecular weight (MW), weaker humification, and higher protein contents. For both BGW and IGW, exposure to solar-simulated radiation led to increases in the E_2/E_3 quotient, biological index (BIX), and ammonium (NH_4^+) and decreases in absorbance, specific absorption coefficient at 254 nm ($SUV\alpha_{254}$), fluorescence index (FI), humification index (HIX), MW, and dissolved organic carbon (DOC). The irradiation also reduced the intensities of humic-like fluorescence peaks and PARAFAC-modeled humic components. On a fractional-absorption-loss basis, the photochemically induced fractional changes in BGW were comparable to those in IGB for $SUV\alpha_{245}$ and E_2/E_3, considerably larger for MW, BIX, and DOC, and substantially smaller for FI and HIX. On an absorbed-photon basis, the efficiencies of absorbance photobleaching and DOC photomineralization for DOM in BGW were 8.3 times and 2.0 times those of the respective photoprocesses for DOM in IGW, while the efficiency of

photoammonification for DOM in BGW was 41% of that for DOM in IGW. Results from this study, in combination with those reported previously for surface waters, lead to a tentative paradigm: terrigenous DOM is more prone to absorbance photobleaching but less prone to photoammonification than microbial-derived DOM while the two DOM pools are comparably reactive with respect to DOC photomineralization. The scientific content of this thesis has been published in Marine Chemistry with the citation of: Qi L, Xie H, Gagné J-P, Chaillou G, Massicotte P, Yang G-P, 2018. Photoreactivities of two distinct dissolved organic matter pools in groundwater of a subarctic island. Marine Chemistry, https://doi.org/10.1016/j.marchem.2018.03.003.

Contents

List of Abbreviations and Symbols

Abbreviation	Meaning
AQY	Apparent quantum yield
BGW	Beach groundwater
BIX	Biological index
CDOM	Chromophoric dissolved organic matter
DIC	Dissolved inorganic carbon
DOC	Dissolved organic carbon
DOM	Dissolved organic matter
DON	Dissolved organic nitrogen
EEM	Excitation and emission matrix
FI	Fluorescence index
FDOM	Fluorescent DOM
F_{max}	Maximum fluorescence intensity
HIX	Humification index
IGW	Inland groundwater
MW	Molecular weight
PARAFAC	Parallel factor
PLA	Percent of light absorbed
R.U.	Raman Units
SGD	Submarine groundwater discharge
UVA	Ultraviolet-A (320-400 nm)
UVB	Ultraviolet-B (290-320 nm)

Symbol	Meaning	Unit
A	Cross-section area of quartz-windowed irradiation cells	m^2
a_{CDOM}	Absorption coefficient of CDOM	m^{-1}
$a_{CDOM,0}$	a_{CDOM} at irradiation time zero	m^{-1}
$a_{CDOM,t}$	a_{CDOM} at irradiation time t	m^{-1}
$a_{Fe}*$	Fe(III)-specific absorption coefficient (epierian)	$L\ mg^{-1}\ m^{-1}$
$AFL_{250-400}$	Average fractional loss of CDOM absorption coefficient from 250-400 nm	dimensionless
$ARF_{250-400}$	Average remaining fraction of CDOM absorption coefficient from 250-400 nm	dimensionless
a_{tot}	Sum of a_{CDOM} and a_w in irradiation cells	m^{-1}
a_{TOT}	Sum of a_{CDOM}, a_w, and absorption coefficient of suspended particles in the groundwater-receiving water body	m^{-1}
a_w	Absorption coefficient of pure water	m^{-1}
E_2/E_3	Ratio of absorption coefficient at 250 nm to that at 365 nm	
L	Light pathlength of quartz-windowed irradiation cells	m
l	Light pathlength of irradiation tubes	m

M_w	Weight-average MW	kDa
M_n	Number-average MW	kDa
n	Number of samples in statistical analysis	dimensionless
N	Dilution factor for DOM discharged from groundwater into the receiving seawater body	dimensionless
Q_0	photon flux just below the front window of quartz-windowed irradiation cells	mol photons m^{-2} h^{-1} nm^{-1}
Q_a	Photons absorbed by CDOM in quartz-windowed irradiation cells	mol photons m^{-2} s^{-1} nm^{-1}
Q_{d0-}	Downwelling solar photon flux just below the surface of the groundwater-receiving body	mol photons m^{-2} d^{-1} nm^{-1}
R^2	Determination of coefficient	dimensionless
$R_{DOC/CDOM}$	Ratio of DOC loss to $AFL_{250-400}$	dimensionless
$S_{275-295}$	Spectral slope coefficient between 275 and 295 nm	μm^{-1}
$SUV\alpha_{254}$	Specific UV absorption coefficient (decadic) at 254 nm	L mg^{-1} m^{-1}
S_λ	Spectral slope coefficient at wavelength centered at λ within an interval of 21 nm	μm^{-1}
Z	Depth of the surface mixed layer or photoactive layer in the groundwater-receiving water body	m
λ	Wavelength	nm
λ_{em}	Fluorescence emission wavelength	nm
λ_{ex}	Fluorescence excitation wavelength	nm
Λ	Action spectra of photobleaching or photoammonification	m^{-1} CDOM m^{-2} s^{-1} or mol NH_4^+ m^{-2} s^{-1}
μ	Mean cosine of photons	dimensionless
Φ_{CDOM}	AQY of CDOM absorbance photobleaching	m^{-1} CDOM (mol photons)$^{-1}$
$\overline{\Phi}_{CDOM}$	Solar irradiance spectrum-weighted mean Φ_{CDOM}	m^{-1} CDOM (mol photons)$^{-1}$
Φ_{DOC}	AQY of photochemical DOC loss	mol DOC (mol photons)$^{-1}$
$\Phi_{NH_4^+}$	AQY of NH_4^+ photoproduction	mol NH_4^+ (mol photons)$^{-1}$
$\overline{\Phi}_{NH_4^+}$	Solar irradiance spectrum-weighted mean $\Phi_{NH_4^+}$	mol NH_4^+ (mol photons)$^{-1}$
ρ	polydispersity	dimensionless
τ_{CDOM}	Photochemical turnover time of CDOM absorbance	d
τ_{DOC}	Photochemical turnover time of DOC	d
τ_{DOM}	Photochemical turnover time of DOM	d
τ_{DON}	Photochemical turnover time of DON	d

List of Tables

List of Figures

Chapter 1. Introduction

1.1.   Dissolved organic matter in submarine groundwater

Submarine groundwater discharge (SGD), which is composed of terrestrial fresh groundwater and recirculated seawater, plays an important role in the ocean's hydrological cycle (Burnett et al., 2001; Moore, 2010). The chemical composition of SGD often differs from that expected from simple mixing of terrestrial and seawater end-members due to active processes of production, removal, and transformation occurring in coastal aquifers (Beck et al., 2007; Chaillou et al., 2016; Santos et al., 2009). Generally, SGD contains elevated concentrations of carbon (Cai et al., 2003; Goñi and Gardner, 2003; Santos et al., 2009), nutrients (Slomp and Van Cappellen, 2004), and trace metals such as iron (Windom et al., 2006) compared with coastal waters, which has been hypothesized to influence major biogeochemical cycles in marginal seas (Moore, 2010). Published studies, albeit limited in numbers, have demonstrated that SGD is highly enriched with dissolved organic carbon (DOC) and thus could be a potentially important source of dissolved organic matter (DOM) to coastal oceans (Goñi and Gardner, 2003; Santos et al., 2009). The source and/or origin of this DOM is, however, not well known. Marine-derived solutes are considered as the main source of DOM in tidal sands (McLachlan and Brown, 2006; Anschutz et al., 2009; Kim et al., 2012). However, terrestrial input and in situ production can be other important sources of DOM in beach groundwater as recently demonstrated by Couturier et al. (2016).

1.2.   Literature review on photochemistry of DOM in groundwater

A large part of the submarine groundwater is delivered directly into shallow water bodies near the shore (Burnett et al., 2003; Johannesson et al., 2011). SGD entering deeper depths may be transported to the surface by buoyancy and physical mixing (e.g. tidal action). DOM, more precisely, its chromophoric component (CDOM), in SGD is thus subject to photooxidation by solar radiation, as is for CDOM in surface water discharged into coastal zones. Exposure of CDOM to sunlight leads to photobleaching, photomineralization, photoammonification, and photoalteration of the bioavailability and chemical structure of DOM including its aromaticity and molecular size (Mopper et al., 2015; Osburn and Morris, 2003; Sharpless and Blough, 2014; Zepp, 2003). CDOM photochemistry thus profoundly impacts the optics and biogeochemical processes in aquatic environments. Despite the recognized ecological and environmental importance of CDOM photochemistry in surface water, little attention has been devoted to understanding the photoreactivity of CDOM in SGD. To our knowledge, there are only two published studies on groundwater DOM photochemistry. Bertilsson et al. (1999) determined photoproduction of dissolved inorganic carbon (DIC), ammonium (NH_4^+), and certain selected carboxylic acids in two groundwater samples collected from a boreal watershed in northern Sweden. Koopmans and Bronk (2002) measured photoproduction of NH_4^+ in groundwater taken from coastal Georgia and South Carolina. To date, the effect of solar irradiation on the optical and chemical properties of groundwater DOM remains largely unknown.

Notably, the photoreactivity of CDOM changes with its origin of formation (Aarnos et al., 2012; Brooks et al., 2006) and light exposure history (Powers and Miller, 2015a;

Sharpless et al., 2014; Vähätalo and Wetzel, 2004). In particular, the dose dependence of many CDOM photoprocesses is mostly restricted to interfaces where unexposed CDOM transits from shaded to unshaded environments such as land-water interface and upwelling zones (Vähätalo and Wetzel, 2004; Zhang et al., 2006). Consequently, surface waters downstream of these interfaces may not be suitable for studying photochemistry of the source material. In this regard, groundwater, which usually experiences little exposure before flowing into open water bodies, offers a good opportunity for examining the dose and source dependences of CDOM photoreactivity.

1.3.   Objectives

Using two groundwater CDOM pools of different origins, this project aims to elucidate

1) the effect of solar radiation on the optical and chemical characteristics of groundwater CDOM,

2) the influence of the source of CDOM on its photochemical behavior in terms of photobleaching, photomineralization, and photoammonification, and

3) the difference in the photochemical turnover of these two groundwater CDOM pools in the receiving coastal water.

Chapter 2. Methods

2.1. Study sites

The sampling site is located on the Martinique Beach of the Îles-de-la-Madeleine in the Gulf of St. Lawrence (Canada) (Figure 1). As part of the Maritimes Permo-Carboniferous Basin in the Northeastern Appalachian Geological Province (Brisebois, 1981), the Îles-de-la-Madeleine are an archipelago encompassing approximately 15 islands, with seven of them joined as tombolos. The core of the main island is composed of interbedded volcanic and volcanoclastic rocks flanked by sandstones of the Cap-aux-Meules formation developed during the Permian Inferior period (Brisebois, 1981). This sandstone formation forms the main aquifer in the archipelago that features high pumping rates due to elevated transmissivities (mean: ~4 × 10^{-3} m^2 s^{-1}) and recharge rates (mean: ~230 mm yr^{-1}, i.e. ~30% of the annual snow and rain precipitation) (Leblanc, 1994; Madelin'Eau, 2004). Groundwater flows from the central volcanic core recharge zone to the unconfined sandstone aquifer and finally to the sea in the form of surficial and submarine discharges.

The archipelago's coasts are mostly fine-grained (~300 μm) sandy barrier systems resulting from the erosion of Holocene deposits and eolian transport. Sediments mainly comprise silicate fragments while the underlying Permian sandstone aquifer contains finer red-orange sands (grain size: ~100 μm) composed of silicate and aluminosilicate with iron-coated silicate grains (Chaillou et al., 2014). At the top of the sandstone aquifer, there is a fragmented organic-rich horizon, with a total organic carbon content of ~20% weight percent. This buried horizon is mainly composed of terrestrial plant detritus that was formed ~900 years B.P., as revealed by ^{14}C age dating (Juneau, 2012) and is a

geological evidence of local and regional submergences over the last millennia (Grant, 1970; Juneau, 2012; Scott et al., 1995). The sandy Martinique Beach acts as a shallow unconfined aquifer at the shoreline and releases diffuse fresh inland groundwater to the coastal water. Within the beach, fresh and cold groundwater flows towards the seaward discharge region below a narrow intruding saline circulation cell located near the top of intertidal sediments (Chaillou et al., 2016). The discharge zone is not well characterized but likely has a narrow zone of ~100 m from the beach face (Chaillou et al., submitted) where fresh SGD fluxes were estimated around 0.03 m^3 s^{-1} based on Darcy's Law (Chaillou et al., 2016). This same study revealed a short groundwater residence time along the subterranean estuary (~32 d), low oxygen conditions (~20% saturation), and a fresh groundwater-born DOC flux of 27 kg d^{-1} at the beach face.
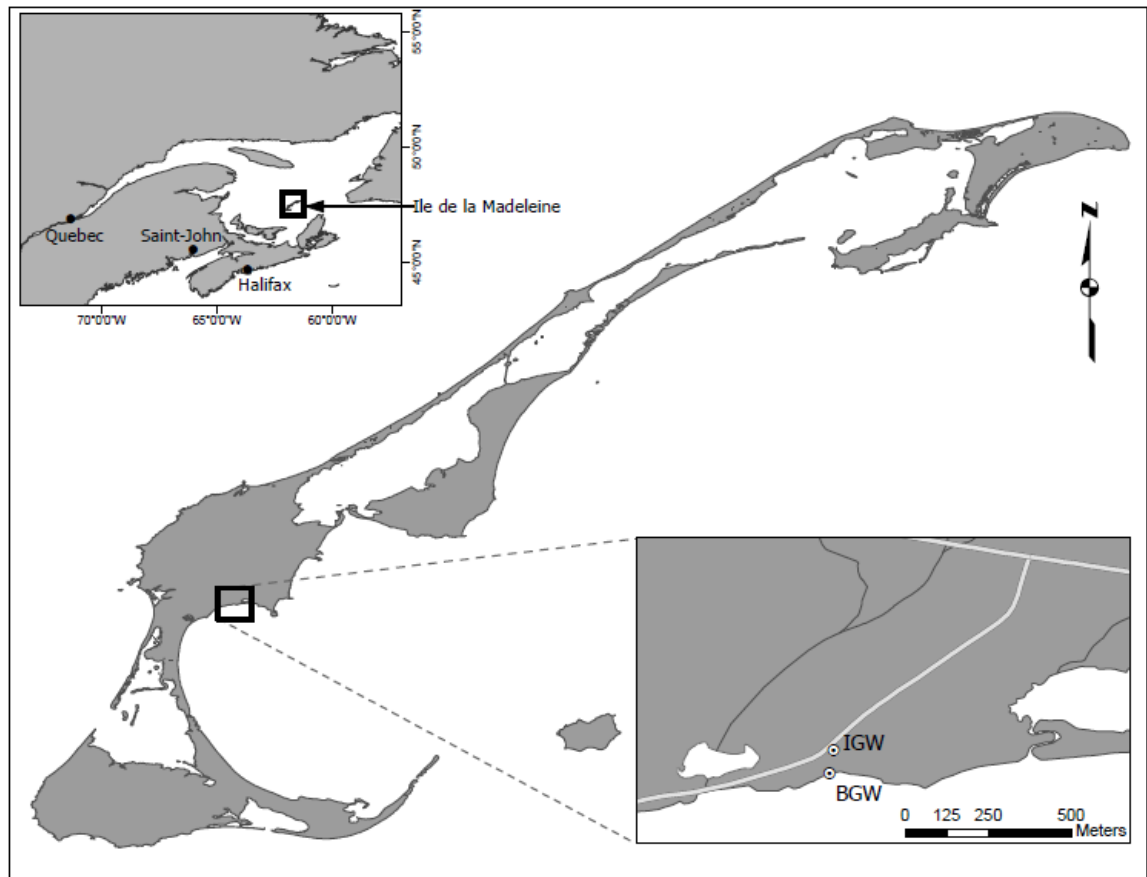
Figure 1. Map of sampling sites.

2.2. Sample collection

Sampling was carried out on the Martinique Beach during the low spring tide period in June 2012, when the unconfined aquifer was supposedly recharged with freshly thawed snow pack. Beach groundwater (BGW) was collected from a site (47.32°N, -65.98°W) ~15 m from the high tide mark (Figure 1) using a multi-level porewater sampler as described by Chaillou et al. (2015). The sampler was installed at least two days before sampling to allow sediments around the sampler to regain equilibrium. Groundwater was pumped from 80 cm below the beach surface into an in-line flow cell fitted with a calibrated YSI 600QS multi-parametric probe to monitor in situ temperature, dissolved oxygen concentration, and salinity. After these parameters had stabilized, groundwater was passed through a Pall AcroPak® 1000 filtration capsule (0.2 µm pore-size polyethersulfone membrane) and collected into two 4-L clear-glass bottles wrapped with black plastic film to avoid light exposure. Because of the relatively high pumping flow rate (~1 L min^{-1}), the collected water was thought to cover all depths that were shallower than 80 cm. In addition to BGW, inland groundwater (IGW) was taken from a 5-m deep residential water well, ~50 m landward from the BGW sampling site (Figure 1), by pumping water (5.0 m deep) to the surface through silicone tubing. As for BGW, IGW was collected only after physiochemical parameters had stabilized, and was filtered and stored in the same manner as for BGW. The sample bottles, closed with PTFE-lined screw caps, were transported to the home laboratory in Rimouski under dark and cool conditions. Before use, the glass bottles were soaked with 10% HCl overnight, thoroughly rinsed with Nanopure water, air-dried, and then combusted at 450 °C for 5 h.

The filtration capsules were flushed with 15 L Nanopure water and conditioned with 2 L sample water.

2.3. Sample irradiation

Immediately before irradiation, sample water was re-filtered through 0.2-µm polyethersulfone membrane filters and transferred into 93-mL cylindrical quartz tubes (i.d.: 2.2 cm; length: 24.5 cm). The tubes were closed with ground-glass stoppers without headspace except where noted. The tubes were horizontally placed in a temperature-controlled water bath (15 ± 1 °C), submerged 0.5 cm below the water surface and irradiated in time series under full-spectrum radiation using a Suntest XLS+ solar simulator equipped with a 1.5 kW xenon lamp. A special UV glass filter was installed to remove UV radiation with wavelengths shorter than 290 nm.

IGW and BGW were irradiated over time courses of 140 h and 474 h, respectively, to examine the temporal trends of photobleaching and DOC photomineralization, and of 96 h and 120 h, respectively, to determine the kinetics of NH_4^+ photoproduction. Duplicate tubes were sacrificed periodically for analyses described in section 2.4. The choice of irradiation time depended on the initial CDOM abundance in the sample (Table 3) and the rate of the photoprocess of interest, with longer irradiations performed for the more colored water and the slower processes. For the 474-h time-course exposure of the highly colored BGW (Table 1), the irradiation tubes were left with 31-mL lab air and gently shaken at each sampling time to mitigate oxygen depletion by photochemical oxygen consumption (Andrews et al, 2000) and to lessen transport limitations on photochemical kinetics due to severe inner filter effects (Hu et al., 2002). The solar simulator's photon fluxes at the irradiation surface were determined with an OL-754 spectroradiometer fitted

with a 2-inch OL IS-270 integrating sphere and calibrated with an OL 752-10E irradiance standard. The photon fluxes in the UVB (280–320 nm), UVA (320–400 nm), and visible (400–600 nm) were 1.5, 1.2, and 1.4 times those of the noontime clear-sky sunlight measured in May at Rimouski (48.453° N, 68.511° W), Canada (Hong et al., 2014). One day of solar-simulated irradiation thus corresponded to 6.0-d UVB, 4.8-d UVA, and 5.7-d visible irradiation with clear-sky sunlight at the latitude of 48.453°N, assuming 1-d clear-sky irradiation to be equivalent to 0.25-d noontime irradiation (Miller and Zepp, 1995).

Additional irradiations were performed to quantify wavelength-resolved apparent quantum yields (AQYs) of photoammonification ($\Phi_{NH_4^+}$), following the method reported by Xie et al. (2012). Briefly, the 0.2-µm re-filtered water was dispensed into quartz-windowed cylindrical cells (i.d.: 2.0 cm; length: 14.0 cm) which were irradiated at a temperature of 15 ± 1 °C using a SUNTEST CPS solar simulator equipped with a 1.5-kW xenon lamp. Six light treatments were obtained with successive Schott long band-pass cutoff filters: WG280, WG295, WG305, WG345, WG395, and WG435. Light exposure lasted for 12 h for both IGW and BGW. Spectral photon fluxes under each cutoff filter were measured with the OL-754 spectroradiometer. The absorbance photobleaching data obtained from these same irradiations were used to derive spectrally resolved AQYs of CDOM photobleaching (Φ_{CDOM}). Parallel dark controls accompanied all light treatments and showed negligible changes in the measured parameters relative to the initial samples

Table 1.

Description of optical indices and EEM peaks used in the text. λ_{ex}: excitation wavelength; λ_{em}: emission wavelength.

Absorbance-based index	Calculation	Function	Reference
$a_{CDOM}(330)$: absorption coefficient at 330 nm (m⁻¹)	2.303 times absorbance at 330 nm divided by the pathlength of the spectrophotometer's cuvette	Indicator of CDOM content; other wavelengths such 325 nm, 350 nm, 375 nm, etc. have also been adopted	Blough and Del Vecchio, (2002); Nelson et al. (2013); Osburn et al. (2009a)
$SUV\alpha_{254}$: specific UV absorption coefficient (L mg⁻¹ m⁻¹)	Decadic (i.e. base 10) absorption coefficient divided by DOC concentration in mg L⁻¹	Indicator of aromatic carbon content of CDOM, with higher values indicating higher aromatic carbon contents	Weishaar et al., 2003
$S_{275-295}$: spectral slope between 275 nm and 295 nm (nm⁻¹)	Exponent of nonlinear fit of an exponential function to the absorption spectrum over the wavelength range from 275 nm to 295 nm	Proxies of average molecular weight and lignin content of CDOM, with higher values indicating lower molecular weights and lower lignin contents	Fichot and Benner (2012); Helms et al. (2008)
E_2/E_3: the E2 to E3 quotient	Ratio of $a_{CDOM}(250)$ to $a_{CDOM}(365)$	Proxies of aromaticity and average molecular weight of CDOM, with higher values indicating lower molecular weights and lower aromaticity	Peuravuori and Pihlaja (1997)

Fluorescence-based index	Calculation	Function	Reference
FI: fluorescence index (dimensionless)	Ratio of emission intensity at 450 nm to that at 500 nm with excitation at 370 nm	Indicator of relative contribution of terrestrial and microbial DOM sources, with higher values indicating higher contributions of microbial-derived DOM	McKnight et al. (2001)
BIX: biological index (dimensionless)	Ratio of emission intensity at 380 nm to that at 430 nm with excitation at 310 nm	Indicator of relative contribution of autochthonous DOM, with higher values indicating high contributions of recently produced DOM of autochthonous origin	Huguet et al. (2009)
HIX: humification index (dimensionless)	Ratio of emission intensity integrated over 435-480 nm to that over 300-345 nm with excitation at 254 nm	Indicator of humic substance content and degree of humification, with higher values indicating higher degrees of humification	Ohno (2002)

EEM peak name	Wavelength	Component	Reference
A	λ_{ex} = 260 nm; λ_{em} = 400–460 nm	UVC humic-like	Coble (2007)
C	λ_{ex} = 320-360 nm; λ_{em} = 420–460 nm	UVA humic-like	Coble (2007)
M	λ_{ex} = 290-310 nm; λ_{em} = 370–410 nm	UVA humic-like	Coble (2007)
T	λ_{ex} = 275 nm; λ_{em} = 340 nm	Protein-like (tryptophan-like)	Coble (2007)
B	λ_{ex} = 275 nm; λ_{em} = 305 nm	Protein-like (tyrosine-like)	Coble (2007)

2.4.   Analyses

2.4.1. Optical analyses

CDOM absorbance was scanned at intervals of 1 nm from 200 nm to 800 nm using a Perkin-Elmer lambda-35 dual beam UV-visible spectrometer fitted with a 1- or 5-cm quartz cuvette and referenced to Nanopure water. The Napierian absorption coefficient, $a_{CDOM}(\lambda)$ (m^{-1}), where λ is wavelength in nanometers, was calculated as 2.303 times the absorbance divided by the pathlength of the cuvette in meters. A baseline correction was made by subtracting the average absorbance between 683 nm and 687 nm from all spectral values (Babin et al., 2003). The decadic specific absorption coefficient at 254 nm (SUVα_{254}), the spectral slope coefficient between 275 nm and 295 nm ($S_{275-295}$), and the E_2/E_3 quotient are calculated from the measured absorption coefficients following the procedures described in Table 1. Furthermore, the wavelength distribution of spectral slope, also termed the spectral slope curve (S_λ), between 250 nm and 550 nm was analyzed at 21 nm intervals with a 1 nm step according to the method of Loiselle et al. (2009). S_λ was computed using non-linear exponential fitting and represents the spectral slope at the center wavelength of a given 21-nm wavelength band.

Fluorescence excitation-emission matrices (EEMs) were obtained using a FLUOROMAX-4 spectrofluorometer to characterize the composition of CDOM (Coble, 1996; Boehme et al., 2004). The bandwidths were set to 5 nm for excitation and 2 nm for emission. A series of emission scans between 280 nm and 560 nm were collected over excitation wavelengths between 240 nm and 500 nm at 5-nm increments. Excitation wavelengths below 240 nm and emission wavelengths below 300 nm were removed due to low signal to noise ratios. Before optical analysis, the samples were allowed to warm

to room temperature. Nanopure water was used as blank to remove most of the first- and second-order Raman scattering. The spectra of all measurements were normalized to Raman Units (R.U.), employing the Raman Scatter Peak correction reported by Lawaetz and Stedmon (2009). BGW samples with high absorbance were diluted with Nanopure water to $a_{CDOM}(280) < 11.3$ m^{-1} to eliminate the inner-filtering effect (Ohno, 2002). Major peaks in the EEMs were identified using the wavelength ranges reported by Coble (2007), and fluorescence (FI), biological (BIX), and humification (HIX) indices are computed from the corrected EEMs per protocols published in the literature (Table 1). Note that Table 1 also lists the biogeochemical functions of the optical indices employed in this study.

Parallel factor analysis (PARAFAC) was performed to decompose the EEMs into a set of underlying fluorescent components (Stedmon et al., 2003; Stedmon and Bro, 2008). To reduce the dominance of high fluorescence intensity signals, the EEMs were first scaled to a unit of variance within the sample mode to construct the calibration model (Bro, 1997). PARAFAC models from 2 to 7 components with constraints of non-negativity in all modes were successively conducted with MATLAB (version 2008b; MathWorks 2008) using DOM Fluorescence Toolbox (DOM Fluor version 1.6) and validated as described by Stedmon and Bro (2008). The parameters obtained from the PARAFAC model were used to calculate an approximate abundance of each component, expressed as F_{max} in R.U., which corresponds to the maximum fluorescence intensity for a particular sample.

2.4.2. Chemical analyses

The molecular weight (MW) of CDOM was determined using high-pressure size exclusion chromatography (HPSEC) according to the protocol method reported by Chin et al. (1994) and modified by Lou and Xie (2006). Briefly, samples (100 μL) were injected at controlled temperature (20°C) into a Waters Protein-Pak 125 column carrying a mobile phase of 0.1 mol L^{-1} sodium chloride aqueous solution buffered with phosphate to pH 6.8. The absorbance of eluents was detected at 254 nm with a Waters 2487 dual-λ absorbance detector. Peak integration was performed using Waters Breeze GPC software. The void volume and total permeation volume of the column were determined using blue dextran and acetone, respectively. The system was calibrated with acetone (MW: 58) and sodium polystyrene sulfonate standards (PPS, Polysciences, MA) with molecular weights of 1.8, 4.6, 8, 18, and 35 kDa. Data from the PPS 1.8 kDa were excluded because it displayed wide multiple peaks, as also reported by Zhou et al. (2000). Calculation of number- and weight-average MW followed the formulae of Chin et al. (1994). The ratio of weight-average MW (M_w) to number-average MW (M_n) gives polydispersity (ρ), a measure of the heterogeneity of CDOM (Chin et al., 1994).

DOC samples were acidified to pH ~2 with 2 N HCl to remove the dissolved inorganic carbon and analyzed in triplicate using a Shimadzu TOC-Vcpn carbon analyzer calibrated with potassium biphthalate. The system was checked, at intervals of seven consecutive sample analyses, against Hansell's low-carbon and deep Florida Strait (700 m) reference waters with DOC concentrations ([DOC]s) of 1 μmol L^{-1} and 41–44 μmol L^{-1}, respectively. The coefficient of variation on five replicate injections was <1.5%.

Determination of NH_4^+ concentrations followed the fluorometric method of Holmes et al. (1999). Samples were mixed with a working regent containing o-phthaldialdehyde

(OPA), sodium sulfite, and sodium borate. The addition of sodium sulfide minimizes potential interference from amino acids (Holmes et al., 1999). The sample and working reagent mixture was allowed to stay in the dark for 2.5 h before its fluorescence was measured with the FLUOROMAX-4 spectrofluorometer. The procedure was calibrated using freshly prepared ammonium chloride aqueous solutions covering concentrations from 0 to 5.0 µmol L^{-1}. Corrections were made for the sample's background fluorescence and matrix effect caused by substances such as sea salts and DOM (Holmes et al., 1999). The precision of NH_4^+ determination was $\pm$ 0.01 µmol L^{-1}.

Fe(II) and Fe(III) concentrations in the unirradiated samples were determined using the ferrozine method originally reported by Stookey (1970) and modified by Viollier et al. (2000). Briefly, a water sample was added with ferrozine and the absorbance at 562 nm was recorded with the Perkin-Elmer lambda-35 spectrometer. The mixture was then amended with hydroxylamine hydrochloride and allowed to react for 10 min to complete the reduction of Fe(III) to Fe(II). An ammonium acetate buffer was added to the mixture and the absorbance at 562 nm was determined again. The concentrations of Fe(II) and Fe(III) were calculated from equations 3 and 4 in Viollier et al. (2000) using the absorbance values recorded before and after the reduction of Fe(III). The procedure was calibrated with Fe(III) standards prepared with FeCl$_3$ and diluted in a NaCl solution to match the sample salinity.

2.4.3. Statistical analyses

Statistical analyses were performed using the linear regression software of SigmaPlot for Windows (version 10.0, Systat Software Inc., 2006).

2.5. Retrieval of spectral AQYs

The spectral AQY of NH_4^+ photoproduction ($\Phi_{NH_4^+}(\lambda)$) is defined as the number of moles of NH_4^+ produced per mole of photons absorbed by CDOM at wavelength λ. The photon flux absorbed by CDOM, $Q_a(\lambda)$ (mol photons m^{-2} s^{-1} nm^{-1}), in an irradiation cell was calculated according to Hu et al. (2002):

$$Q_a(\lambda) = AQ_0(\lambda)a_{CDOM}(\lambda)(a_{tot}(\lambda))^{-1}(1 - \exp(-a_{tot}(\lambda)L)) \quad (1)$$

where A (m^{-2}) and L (m) denote the cross-sectional area and pathlength of the irradiation cells, respectively, $Q_0(\lambda)$ (mol photons m^{-2} s^{-1} nm^{-1}) signifies the photon flux just below the front window of the cell, and $a_{tot}(\lambda)$ (m^{-1}) is the sum of $a_{CDOM}(\lambda)$ and the absorption coefficient of pure water at wavelength λ taken from Pope and Fry (1997) and Buiteveld et al. (1994). $\Phi_{NH_4^+}(\lambda)$ is assumed to decrease with wavelength quasi-exponentially (Xie et al., 2012):

$$\Phi_{NH_4^+}(\lambda) = m_1 \exp(m_2 (\lambda + m_3)^{-1}) \quad (2)$$

where m_1, m_2, and m_3 are fitting parameters. The amount of produced in an irradiation cell over the exposure period can then be predicted as the product of the assumed function and the number of photons absorbed by CDOM integrated from 290 nm to 600 nm. The optimum values of the unknown parameters in Eq. 2 are obtained using an Matlab-coded iterative curve-fit method (Johannessen and Miller, 2001; Zhang et al., 2006) by varying these parameters from initial estimates until the minimum difference between the measured and predicted production is achieved.

The spectral AQY of CDOM absorbance photobleaching ($\Phi_{\text{CDOM}}(\lambda)$) was calculated as the loss of CDOM absorption coefficient at 330 nm ($a_{\text{CDOM}}(330)$) per mole of photons absorbed by CDOM at wavelength λ (Osburn et al., 2009). In the calculation of $\Phi_{\text{CDOM}}(\lambda)$, $a_{\text{CDOM}}(330)$ is assigned the units of m^{-1} CDOM per m^3 water (Vähätalo and Wetzel, 2004; Osburn et al., 2009a). $\Phi_{\text{CDOM}}(\lambda)$ was modeled using Eq. 2 in the same manner as $\Phi_{\text{NH}_4^+}(\lambda)$. Based on R^2 and the normalized root-mean-square error for the regression of the photochemical rates calculated from the retrieved $\Phi(\lambda)$ against the measured rates (Koehler et al., 2016), the quasi-exponential function of Eq. 2 performed better than the simple exponential form (e.g. Vähätalo and Wetzel, 2004) for both BGW and IGW, though the difference for BGW photobleaching was marginal (Table 2). The quasi-exponential model was thus chosen for this study. Note that AQYs have units of mol NH_4^+ (mol photons)$^{-1}$ for photoammonification and m^{-1} CDOM (mol photons)$^{-1}$ for photobleaching. For brevity, these units are omitted herein.

Table 2.
Comparison of the simple exponential and quasi-exponential models for deriving apparent quantum yield spectra of absorbance photobleaching and photoammonification. nRMSE and R^2 are normalized root-mean-square error and coefficient of determination, respectively, for the regression of modeled against measured rates. Simple exponential model is signified by $\Phi(\lambda) = m_1\exp(-m_2(\lambda - 290)$ and quasi-exponential model by $\Phi(\lambda) = m_1\exp(m_2(\lambda + m_3)^{-1})$, where $\Phi(\lambda)$ denotes apparent quantum yield at wavelength λ (nm), 290 is the reference wavelength in nanometers, and m_1, m_2, and m_3 are fitting parameters.

	Photobleaching				Photoammonification			
	BGW		IGW		BGW		IGW	
Model	R^2	nRMSE (%)	R^2	nRMSE (%)	R^2	nRMSE (%)	R^2	nRMSE (%)
Simple exponential	0.986	9.2	0.843	17.1	0.983	13.3	0.982	11.2
Quasi-exponential	0.988	8.2	0.978	6.2	0.997	5.4	0.993	6.7

To evaluate the relative contributions of different spectral regimes to photobleaching and photoammonification under natural solar radiation, action spectra ($\Lambda(\lambda)$) of these two photoprocesses are calculated according to Song et al. (2013):

$$\Lambda(\lambda) = Q(\lambda)\Phi(\lambda) \qquad (3)$$

where $\Phi(\lambda)$ denotes $\Phi_{NH_4^+}(\lambda)$ or $\Phi_{CDOM}(\lambda)$ and $Q(\lambda)$ (mol photons m^{-2} s^{-1} nm^{-1}) is the noontime clear-sky solar photon flux recorded at Rimouski (48.453° N, 68.511° W), Canada, on 24 May 2005. $\Lambda(\lambda)$ signifies the spectral distribution of the depth-integrated photobleaching (m^{-1} CDOM m^{-2} s^{-1}) or photoammonification (mol NH_4^+ m^{-2} s^{-1}) rate in an idealized water column in which CDOM is the sole light absorber. Moreover, to facilitate comparison of AQY spectra between different samples, a solar spectrum-weighted mean AQY($\bar{\Phi}$) is defined following Zhang et al. (2006):

$$\bar{\Phi} = \int_{290}^{600} Q(\lambda)\Phi(\lambda)d\lambda \left(\int_{290}^{600} Q(\lambda)d\lambda \right)^{-1} \qquad (4)$$

where $\bar{\Phi}$ denotes $\bar{\Phi}_{CDOM}$ or $\bar{\Phi}_{NH_4^+}$ with $\Phi(\lambda)$ corresponding to $\Phi_{NH_4^+}(\lambda)$ or $\Phi_{CDOM}(\lambda)$. This normalization reduces the full AQY spectrum to a single value equivalent to the loss of a_{CDOM} or the production of NH_4^+ divided by the amount of photons absorbed by CDOM in the idealized water column delineated above. $\bar{\Phi}$ accounts for both the magnitudes and shapes of the AQY and solar irradiance spectra, thereby giving more weights to the wavelengths at which the values of $\Lambda(\lambda)$ are elevated.

Chapter 3. Results and Discussion

For brevity, sample names for a property will be added, whereby needed, as a superscript to the right side of the symbol or abbreviation representing that property. For example, $SUV\alpha_{254}^{BGW}$ denotes $SUV\alpha_{254}$ for BGW, while $SUV\alpha_{254}^{IGW}$ stands for $SUV\alpha_{254}$ for IGW. It is further stipulated that each symbol and abbreviation, where applicable, can be used as both a singular and a plural form.

3.1.   Initial sample properties and sources of DOM

3.1.1.   Chemical properties

Table 3 summarizes results from chemical and optical analyses before irradiation. IGW was essentially freshwater (salinity: 0.31) but BGW contained significant amounts of salts (salinity: 2.82) due to entrainment of recirculated seawater (Chaillou et al., 2014; Couturier et al., 2016). In situ temperatures of the two samples (~11-12 °C) were similar but BGW contained much lower dissolved oxygen (~15% saturation) than did IGB (~64% saturation). The pH^{IGW} (6.86) was marginally below the neutral level, whilst pH^{BGW} (6.29) was more acidic, consistent with the reducing condition of BGW as reflected by its lower dissolved oxygen level. Total dissolved Fe in BGW (332.7 μmol L^{-1}) was 261 times higher than in IGW (1.3 μmol L^{-1}), with Fe (III) accounting for 79% and 95% of the total Fe in BGW and IGW, respectively. The far higher total Fe in BGW was due apparently to its reducing condition combined with a highly elevated DOC load (see below), since the solubility of iron is higher under reducing conditions and Fe complexes with DOM (Deflandre et al., 2002).

Table 3.

Physical, chemical, and optical properties of beach groundwater (BGW) and inland groundwater (IGW) before irradiation. Dissolved oxygen (O_2), temperature (T), pH, and salinity were measured in situ. Numbers in parentheses are relative deviations of duplicate samples (%).

Sample	O_2 (μmol L^{-1})	T (°C)	pH	Salinity	Total Fe (μmol L^{-1})	DOC (μmol L^{-1})	$a_{CDOM}(330)$ (m^{-1})	$S_{275-295}$ (μm^{-1})	E_2/E_3	SUVα_{254} (L mg^{-1} m^{-1})	M_w (kDa)	M_n (kDa)	ρ	FIX	BIX	HIX
BGW	50.0	12.4	6.29	2.82	332.7 (0.2)	6094 (0.8)	389.2 (0.07)	11.8 (2.6)	3.94 (0.2)	5.39	3.2	0.56	5.67	1.20	0.38	29.9
IGW	220.0	11.1	6.86	0.31	1.3 (1.5)	196 (1.6)	4.36 (4.0)	15.4 (0.6)	7.93 (0.4)	2.85	1.0	0.34	2.97	1.61 (0.8)	0.70 (0.2)	6.65 (0.1)

BGW (6094 µmol L^{-1}) exceeded IGW (196 µmol L^{-1}) in DOC concentration by a factor of 31. Similarly, DOC^{BGW} was 43 times higher than that in the seawater endmember (140 µmol L^{-1}; Courtier et al., 2016), implying a localized source of DOM in BGW. The extremely high DOC stock in BGW has been ascribed to DOC leached from the paleosol horizon overlying the sandstone aquifer in the beach area (Chaillou et al., 2014, 2015; Courtier et al., 2016). This old-age, forest-soil horizon is carbon-rich (20% total organic carbon by weight; Couturier et al., 2016) and was ^{14}C-dated to ~900 BP (Juneau, 2012). M_W^{BGW} (3.2 kDa) was more than triple M_W^{IGW} (1.0 kDa). M_W^{BGW} falls in the M_W range between Suwanee River fulvic (1.39 kDa) and humic (3.94 kDa) acids (Lou and Xie, 2006) but is closer to the latter; M_W^{IGW} is, nonetheless, below the value of Suwanee River fulvic acid and at the boundary of low- and high-MW DOM. Hence, humic acids were likely the main component of DOM^{BGW}, while light fulvic acids were the dominant fraction of DOM^{IGW}. Moreover, ρ^{BGW} (5.67) was nearly two times higher than ρ^{IGW} (2.97), suggesting a higher heterogeneity of DOM^{BGW} relative to DOM^{IGW}.

3.1.2. Absorption properties

Compared with DOC, the difference in a_{CDOM} between the two samples was even larger, reaching a factor of ~89 at 330 nm (Table 3). As a result, SUVa_{254_BGW} (5.39 L mg^{-1} m^{-1}) was nearly twice SUVa_{254}^{IGW} (2.85 L mg^{-1} m^{-1}), suggesting a much richer aromaticity of CDOM^{BGW} (Ghernaout, 2014; Weishaar et al., 2003). Although a_{CDOM} for both samples decreased about exponentially with wavelength, the absorption spectrum of IGW was markedly steeper than that of BGW (Figure 2A) and S_λ^{IGW} was higher than S_λ^{BGW} (Figure 2B). Both spectral slope curves possessed a broad elevation from ~300 nm

to ~440 nm superimposed with smaller peaks but the elevation was less pronounced for BGW (Figure 2B), again implying a greater proportion of humic acids in BGW than in IGW (Loiselle et al., 2009). The percent difference between the two curves varied greatly with wavelength, exhibiting a deep trough centered at ~287 nm, a double-peak elevation from 320 nm to 367 nm, and lower values in the visible (Figure 2B). $S_{275-295}$ (centered at 285 nm in Figure 2B) for IGW (15.4 μm^{-1}) surpassed that for BGW (11.8 μm^{-1}) by 30.5% but the difference was among the smallest in the UV regime. The commonly adopted wavelength band of 275-295 nm is thus not optimal for describing the spectral difference of our samples. The steeper slope of IGW also led to E_2/E_3^{IGW} (7.93) being twofold higher than E_2/E_3^{BGW} (3.94). The lower values of $S_{275-295}$ and E_2/E_3 for BGW are consistent with the higher M_w^{BGW} described above. The E_2/E_3 values here were used to estimate M_w based on the empirical relationship between M_w and E_2/E_3, $M_w = 0.315*\exp(4.96/(-1.72+E_2/E_3))$, established by Lou and Xie (2006), giving M_w^{BGW} of 2.93 kDa and M_w^{IGW} of 0.70 kDa. These values are close to the measured ones (3.2 kDa for BGW and 1.0 kDa for IGW), validating E_2/E_3 as an indicator of MW in this study.
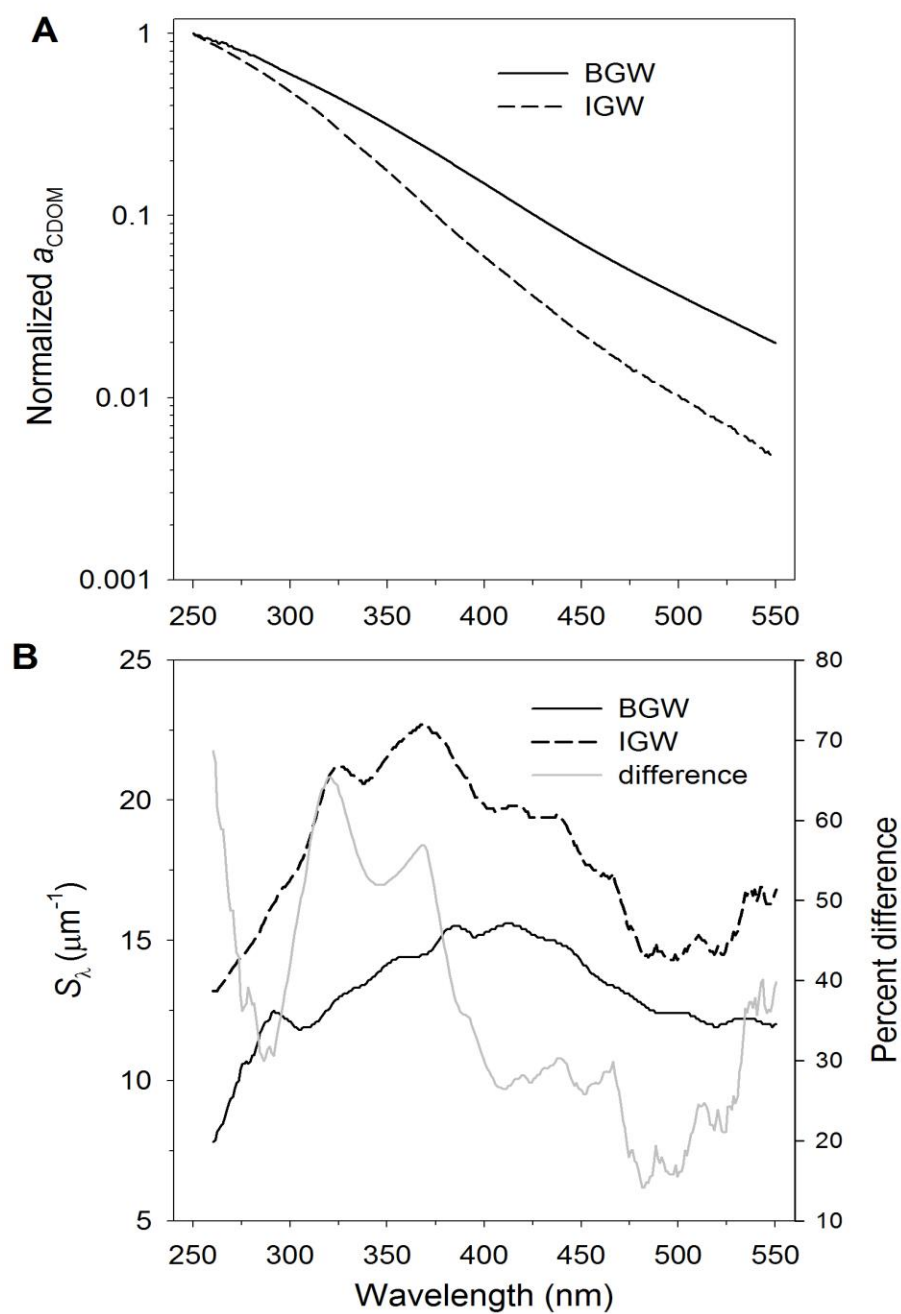
Figure 2. Normalized CDOM absorption coefficient spectra (A) and spectral slope curves (B) for original (unirradiated) samples. Percent difference in panel B is defined as (IGW – BGW) / IGW *100.

3.1.3. Fluorescence properties

FI^{BGW} (1.20) and BIX^{BGW} (0.38) were considerably lower than FI^{IGW} (1.78) and BIX^{IGW} (0.70), while HIX^{BGW} (29.9) exceeded HIX^{IGW} (6.65) by 4.5 times. In general, FI values of less than 1.4 point to DOM of terrestrial origin and values of 1.9 or higher represent DOM of microbial origin (Birdwell and Engel, 2010; McKnight et al., 2001). BIX values ranging from 0.8 to 1.0 indicate fresh, microbially derived DOM, while values below 0.6 signify little autochthonous material (Huguet et al., 2009). Fresh DOM derived from plant biomass usually displays HIX values of <5 (Sazawa et al., 2011), whereas soil-derived DOM has values between 10 and 30 (Wickland et al., 2007). Clearly, the fluorescence indices of BGW are in line with the values for old, soil-derived DOM, while those of IGW are at the borderline between CDOM of terrestrial and microbial origins but closer to the latter.

The EMMs of BGW and IGW both displayed two marked fluorescence peaks (Figure 3A,B), corresponding to peaks A and C defined by Coble (2007) (Table 1). The two peaks were well separated for IGW but largely connected together for BGW. Peak A for IGW blue-shifted by 10 nm in excitation and 16 nm in emission relative to peak A for BGW. These blue shifts imply lower degrees of substitution and conjugation of aromatic moieties in IGW (Stedmon and Nelson 2015), in accordance with the lower MW and $SUV\alpha_{254}$ values for IGW. The intensities of peaks A and C for BGW (33.27 R.U. and 26.20 R.U.) were 59 and 71 times those for IGW (0.56 R.U. and 0.37 R.U.). The ratio of peak C to A for BGW (0.79) was 20% higher than that for IGW (0.66), indicating a higher proportion of humic acid-like *vs.* fulvic acid-like material in BGW compared with IGW (Chen et al., 2003; Hansen et al., 2016). In addition to the evident peaks of A and C,

IGW also exhibited relatively weak fluorescence signals at $\lambda_{ex}/\lambda_{em}$ 240-270 nm/330-380 nm that were partially overlapped by the periphery of peak A. This EEM region, albeit outside peak B and T defined by Coble (2007) (Table1, Figure 3), falls into EEM Region IV corresponding to soluble microbial by-product-like material (Chen et al., 2003). Residual and split-half PARAFAC analyses (Stedmon and Bro 2008) demonstrated that five distinct components, C1−C5 (Figure 4), explained 99.8% of the variance and thus adequately modeled different fluorescent DOM (FDOM) profiles in the dataset combining BGW and IGW both before and after irradiation. The maximum fluorescence intensities (F_{max}) of C1-C4 in the initial BGW were 21.9 R.U. (C1), 17.2 R.U. (C2), 17.8 R.U. (C3), and 9.6 R.U. (C4), while C5 was undetectable ($F_{max} = 0$ R.U.). All five components were detected in the initial IGW, with F_{max} of 0.23 R.U. (C1), 0.13 R.U. (C2), 0.29 R.U. (C3), 0.30 R.U. (C4), and 0.25 R.U. (C5). The abundances of C1, C2, C3 and C4 were thus 96, 130, 61, and 31 times higher in BGW than in IGW. Based on the percent contribution of each individual component (excluding C5) to the summation of C1-C4 (Figure 15), BGW was enriched with C1 and C2 (particularly C2) but depleted with C3 and C4 (particularly C4) relative to IGW. According to previous studies (Cobble, 1996; Stedmon et al., 2003; Massicotte and Frenette, 2011), C1 and C2 represent terrestrial humic-like FDOM, C3 and C4 autochthonous humic-like FDOM and C5 autochthonous protein-like FDOM. PARAFAC modeling thus suggests that DOM[BGW] originated primarily from terrestrial plants while DOM[IGW] was derived principally from microbial processes and thus enriched with proteins, although both DOM pools possessed mixed terrestrial and autochthonous signatures.
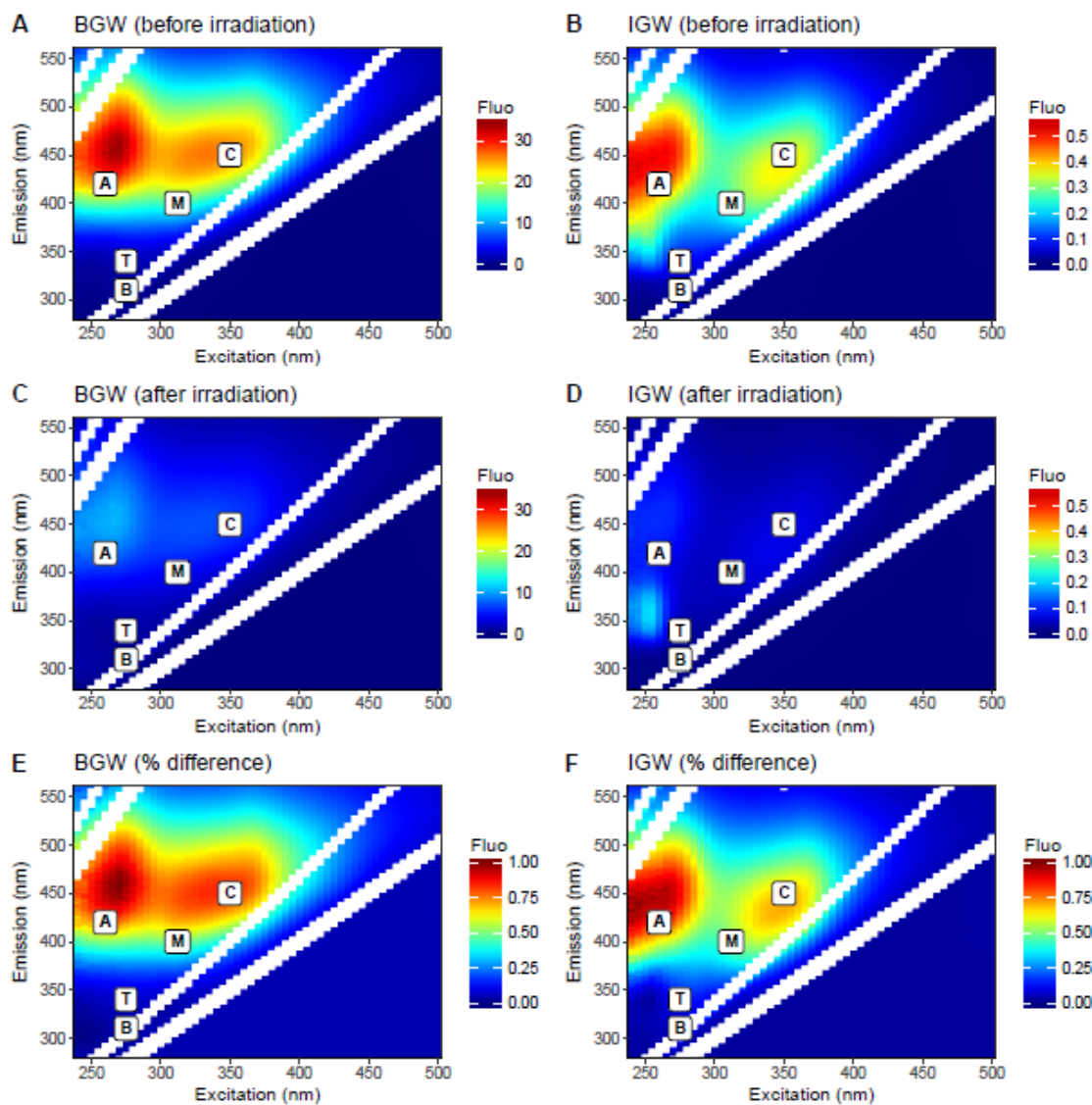
Figure 3. Excitation-emission matrices (EMMs) before and after irradiation for BGW (A and C) and IGW (B and D). Before-after differences are shown in panels E (BGW) and F (IGW). The positions of the EMM peaks defined by Coble (2007) (Table 1) are also displayed. Irradiation lasted for 474 h for BGW and 140 h for IGW.
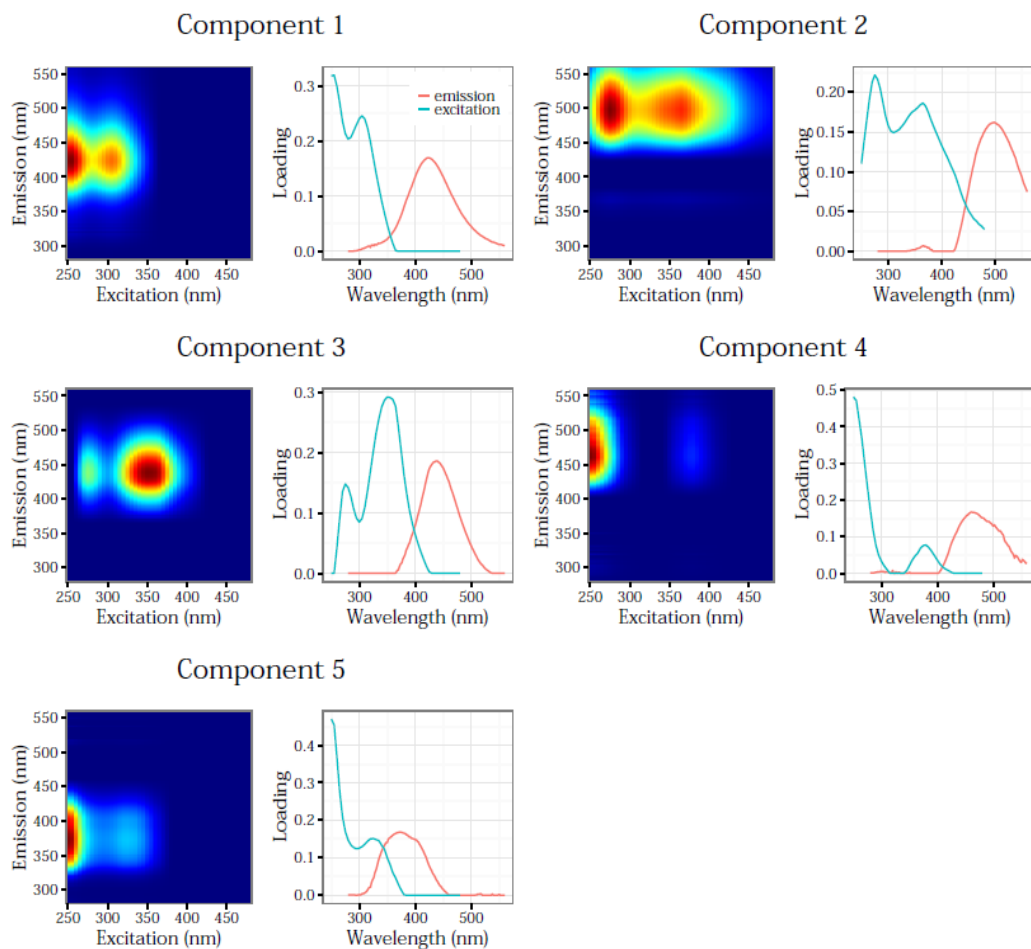
Figure 4. Excitation-emission contours of five components identified by PARAFAC modeling (left panels) and split-half validations of excitation and emission loadings (right panels).

3.1.4. Sources of DOM

Taken together the absorption indicators (SUVα_{254}, S_λ, E_2/E_3), fluorescence indices (FI, BIX, HIX), EEM peaks, PARAFAC components, and MW values, it can be inferred that BGW predominantly contained old DOM of terrestrial origin characterized by large molecular size, high aromaticity, and strong humification, whereas IGW mostly comprised fresh, microbially derived DOM typically having smaller molecular size, lower aromaticity, and weaker humification. A dominant terrestrial origin for DOM^{BGW} is consistent with the proposition of a paleosol source noted above, though microbial production occurring along the groundwater flow path could also have contributed to some extent to the DOM pool in the intertidal area (Couturier et al., 2016). For IGW, its DOM signature might also be influenced by the hydrological, physical, and biogeochemical processes taking place in the overlying soil column. Generally, surface plant litter and soil are significant sources of DOM in groundwater (Baker et al., 2000; Shen et al., 2015). Precipitation drives the transport of DOM down to the saturated zone of the soil column. Selective adsorption of high-MW DOM such as lignin-derived phenols onto soil minerals in the unsaturated zone diminishes the aromaticity of DOM reaching the saturated zone (Shen et al., 2015). The chemical composition and optical properties of this diagenetically altered soil DOM tend to resemble those of microbially derived DOM. Aquifers in the Martinique Beach at the time of sampling (June) were recently recharged with snowmelt (Chaillou et al., 2014). Hence, in addition to DOM microbially produced in the aquifer and/or from the overlying soil column, the DOM^{IGW} could partly originate from the diagenetically modified DOM from the surface soil.

28

3.1.5. Potential interference of iron

The presence of significant Fe(III) can interfere with the optical properties of CDOM, since Fe(III) absorbs both UV and visible radiation (Weishaar et al., 2003; Xiao et al., 2013; Poulin et al., 2014). Xiao et al. (2013) reported Fe(III)-specific absorption coefficients ($a_{Fe}*$) over a broad wavelength range from 320 nm to 650 nm at 1-nm intervals, while Poulin et al. (2014) published $a_{Fe}*$ values at individual wavelengths of 254 nm, 280 nm, 350 nm, and 400 nm. Both groups found little dependence of $a_{Fe}*$ on the source and characteristics of DOM with which Fe(III) is associated. The $a_{Fe}*$ values obtained by Poulin et al. (2014) agreed well with those by Xiao et al. (2013) at 350 nm and 400 nm but are somewhat higher (~15%) than the values at 254 nm and 280 nm extrapolated from the results of Xiao et al. (2013)(错误!未找到引用源。). Based on the Fe(III) concentrations reported in Section 3.1.1, we estimated the effects of Fe(III) on the absorbance-based indicators in our samples using $a_{Fe}*$ values determined by Poulin et al. (2014) (254 nm for SUVα_{254}) and by or extrapolated from Xiao et al. (2013) (330 nm for $a_{CDOM}(330)$, 250 nm and 365 nm for E$_2$/E$_3$, and 275-295 nm for $S_{275-295}$). The results are summarized in Table 4. For the Fe-rich BGW, the correction lowers $a_{CDOM}(330)$ and SUVα_{254} by 30.8% and 24.4% and raises $S_{275-295}$ and E$_2$/E$_3$ by 16.1% and 23.0%. For the Fe-poor IGW, the effect is considerably weaker, reducing $a_{CDOM}(330)$ and SUVα_{254} by 12.6% and 6.7% and increasing $S_{275-295}$ and E$_2$/E$_3$ by 5.2% and 16.6%. Despite the differing extents of the iron effect, the relative differences in these indicators between the two samples are not affected to a large extent by the Fe-corrections (Table 4). In terms of absolute values, the corrected SUVα_{254}^{BGW} (4.07 L mg^{-1} m^{-1}) is still comparable to those

of humic substances extracted from highly colored fluvial waters (Weishaar et al., 2003;

Poulin et al., 2014). The after-correction M_w estimated from
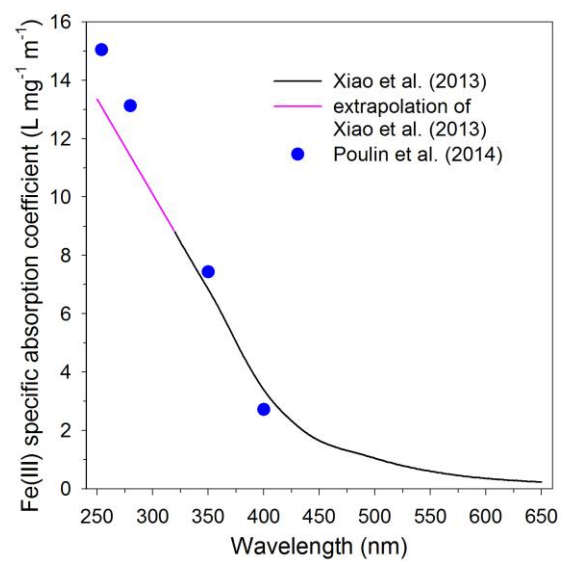
Figure 5. Fe(III) specific absorption coefficient (*e*-based) published by Xiao et al. (2013) and Poulin et al. (2014). Specific absorption coefficients at <320 nm are linearly extrapolated from the data of Xiao et al. (2013) over 320-350 nm.

the M_w-E_2/E_3 relationship of Lou and Xie (2006) is 1.53 kDa for BGW and 0.61 kDa for IGW. M_w^{BGW} decreases by almost 50% compared with the before-correction estimate (2.93 kDa) but remains within the high-molecular-weight class. The change in M_w^{IGW} (0.70→0.61 kDa) is much milder but pushes it towards the lower territory within the low-molecular-weight category.

The interference of Fe with fluorescence depends on various factors, including the ratio of Fe to DOC concentration, CDOM composition, pH, etc., rendering it difficult to quantitatively correct this artifact (Aiken, 2014; Poulin et al., 2014). Given the very low total Fe:DOC ratio in IGW (0.030 mg Fe (mg C)$^{-1}$), the Fe interference in this sample should be minor (Cory, 2005; Poulin et al., 2014). The highly elevated total Fe:DOC ratio in BGW (0.25 mg Fe (mg C)$^{-1}$) made the Fe effect potentially important. However, this effect usually decreases the total fluorescence intensity, increases FI, and preferentially quenches the humic regions of the EEM spectra (i.e. peaks A and C) and the PARAFAC-derived terrestrial humic components (here C1 and C2) (Aiken, 2014; Poulin et al., 2014). Hence, excluding the Fe effect in BGW would further widen the differences between BGW and IGW in the fluorescence properties determined by this study and their implications for characterizing the source of DOM. To sum up, the potential Fe interferences with absorbance and fluorescence should not change the conclusions reached in section 3.1.4 regarding the sources and characteristics of DOM in BGW and IGW.

Aside from Fe, nitrate and nitrite are also UV-absorbers (Mack and Bolton, 1999) and thus may interfere with CDOM absorbance at elevated concentrations. Yet the aggregate nitrate and nitrite concentration is <100 µmol L^{-1} in IGW and <10 µmol L^{-1} in

BGW (Couturier et al., 2017), making them unlikely to significantly affect the absorption

spectra and the absorbance-based indicators in this study (Weishaar et al., 2003).

Table 4.
Effects of iron on the optical properties of the groundwater samples.

	$a_{CDOM}(330)$ (m^{-1})			$S_{275-295}$ (μm^{-1})			E_2/E_3			SUVα$_{254}$ (L mg^{-1} m^{-1})		
	BGW	IGW	BGW/IGW	BGW	IGW	BGW/IGW	BGW	IGW	BGW/IGW	BGW	IGW	BGW/IGW
Before correction (BC)	389.2	4.36	89.2	11.8	15.4	0.77	3.94	7.93	0.50	5.39	2.85	1.89
After correction (AC)	269.5	3.82	70.6	13.7	16.2	0.84	4.85	9.24	0.52	4.07	2.66	1.53
(AC-BC)/BC*100	-30.8	-12.6		16.1	5.2		23.0	16.6		-24.4	-6.6	

3.2.   Photobleaching of absorbance

3.1.6.   Absorption coefficients

Irradiation resulted in loss of a_{CDOM} throughout the UV and visible regimes for both BGW and IGW, but their spectral patterns of percent loss of a_{CDOM} differed (Figure 6). While IGW displayed a marked elevation over 280-350 nm, BGW illustrated a much gentler wavelength dependence characterized by a mild convex at halfway exposure and a slightly tilted line after the entire exposure period. At the end of irradiation, a_{CDOM}^{BGW} lost 97.3% and 99.4% in the UV (250-400 nm) and visible (400-550 nm) ranges, respectively. As the contributions of Fe(III) to a_{CDOM}^{BGW} are estimated to be 29.6% and 40.9% in corresponding wavelength bands, either most Fe(III) was photochemically reduced to non-absorbing Fe(II) (Blough and Zepp, 1995; Doane and Horwáth, 2010) or the contributions of Fe(III) to absorption are overestimated. The percent losses of a_g^{IGW} were considerably smaller, being 64.7% in the UV and 50.7% in the visible. The lower losses in IGW were partly due to its shorter exposure duration (see Chapter 2.3). The very low initial CDOM absorption in IGW (Table 3) made it difficult to precisely determine a_{CDOM} after longer exposures with the conventional spectrophotometer used in this study.

Absorption coefficients at single UV wavelengths, such as 325 nm (Nelson et al., 2013), 330 nm (Osburn et al., 2009a), 350 nm (Miller and Zepp, 1995), and 375 nm (Blough and Del Vecchio, 2002), have been frequently used as a measure of CDOM content and photobleaching. As photobleaching alters the spectral slope of CDOM absorption spectra (e.g. Helms et al., 2008, 2013; Sharpless and Blough, 2014), single wavelengths may not be ideal for quantifying photobleaching. Alternatively, some studies reported photobleaching at several wavelengths (e.g. Osburn et al., 2009b) or using

absorption coefficients integrated or averaged over broad wavelength ranges (Vähätalo and Wetzel, 2004; Osburn et al., 2009b; Porcal et al., 2014). In this study we use the average remaining fraction of a_{CDOM} over 250-400 nm, $ARF_{250-400}$, or its corresponding fractional loss $AFL_{250-400}$, to quantify photobleaching of absorbance. $ARF_{250-400}$ and $AFL_{250-400}$ are defined as follows:

$$ARF_{250-400} = 151^{-1} \sum_{\lambda=250}^{400} \left(a_{CDOM,t}(\lambda) \left(a_{CDOM,0}(\lambda) \right)^{-1} \right) \quad (4)$$

$$AFL_{250-400} = 1 - ARF_{250-400} \quad (5)$$

where $a_{CDOM,t}$ stands for a_{CDOM} at irradiation time t and $a_{CDOM,0}$ for a_{CDOM} at time zero (dark controls showed negligible changes in a_{CDOM}). The 250-400 nm interval was chosen because a_{CDOM} in this band could be more accurately determined than in the visible range and because the percent loss of a_{CDOM} for IGW in the UV was higher than that in the visible (Figure 6). Note that results and conclusions based on $ARF_{250-400}$ (and $AFL_{250-400}$) should be similar to those based on a_{CDOM} at individual wavelengths or averaged over broad wavelength bands, since $ARF_{250-400}$ is well correlated with the latter parameters (Figure 7 and Figure 8).
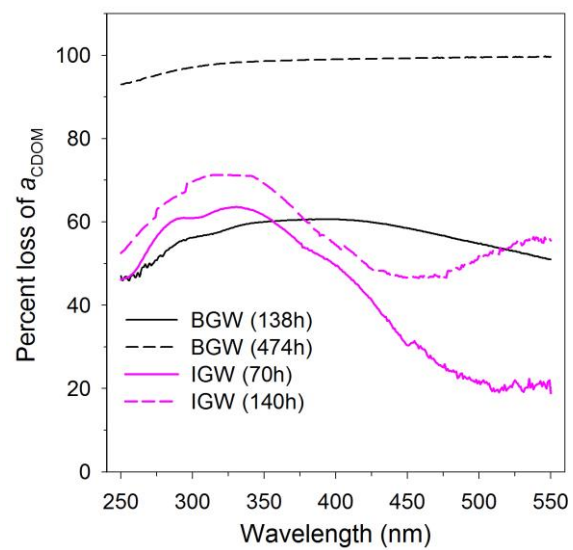
Figure 6. Spectral distribution of percent loss of CDOM absorption coefficient at selected irradiation times.
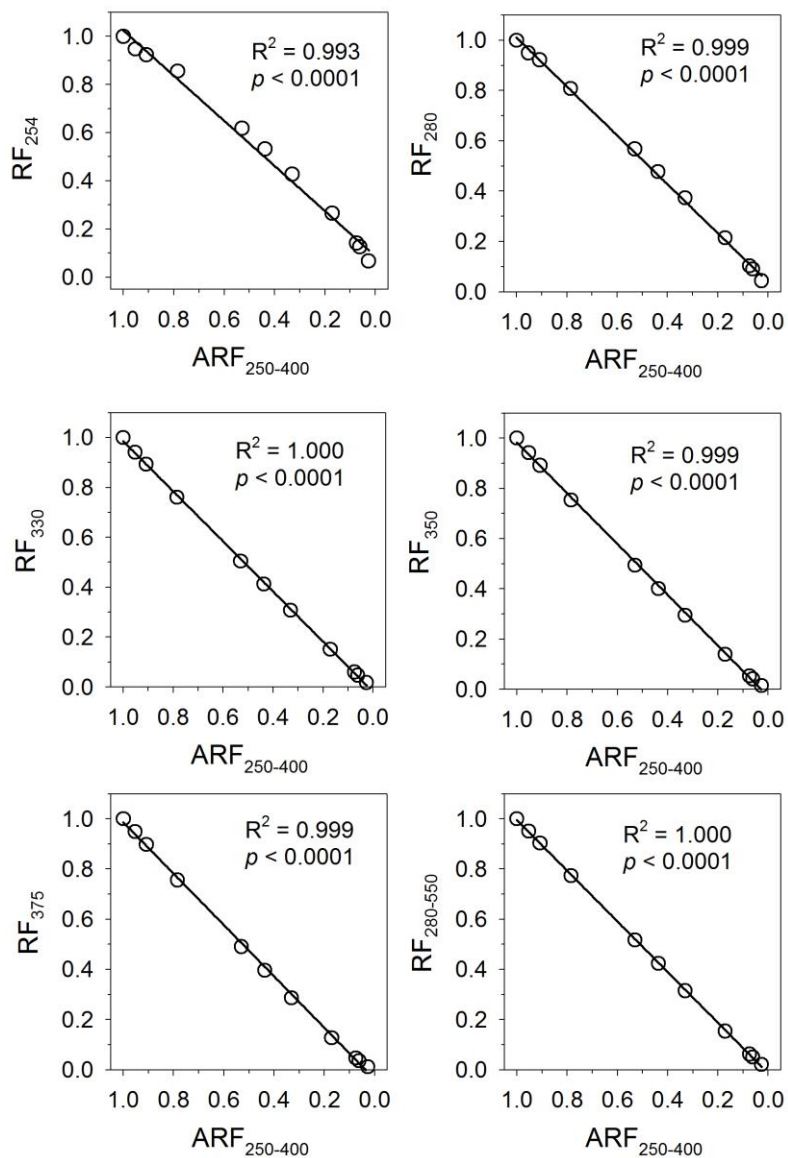
Figure 7. Linear correlation between the remaining fraction of CDOM absorption coefficient at selected individual wavelengths (RF_λ) and the average remaining fraction of CDOM absorption coefficient over 250−400 nm ($ARF_{250-400}$) for beach groundwater (BGW). See Eq. 4 in the main text for the definition of $ARF_{250-400}$. Y-axis $RF_{280-550}$ of the right bottom panel represents the remaining fraction of the mean CDOM absorption coefficient over 280−550 nm.
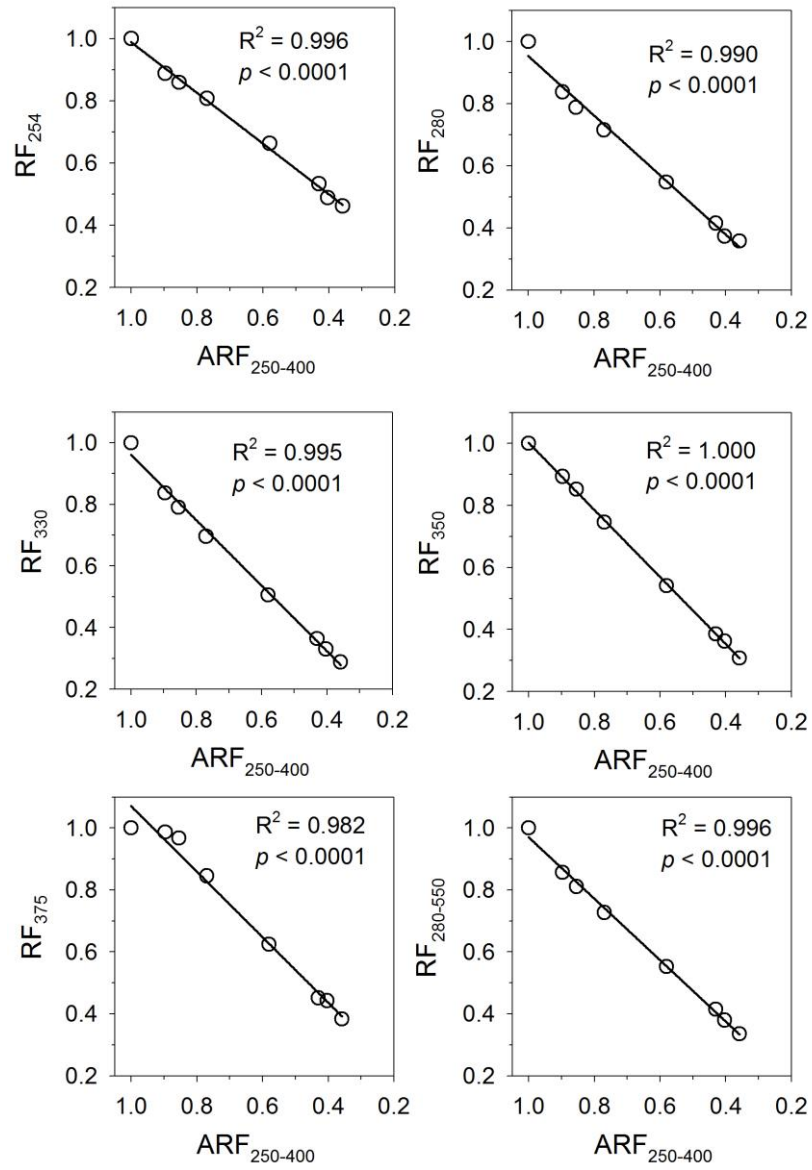
Figure 8. Same as in Figure 7 except for inland groundwater (IGW)

ARF$_{250-400}^{BGW}$ decreased with irradiation time linearly during the first 210 h and exponentially after that (Figure 10). The extremely high absorption of BGW caused strong self-shading (Figure 9) which could have led to the zero-order kinetics observed during the first half of the irradiation (Miller, 1998). ARF$_{250-400}^{IGW}$ declined exponentially throughout the exposure period but the rate constant almost halved during the last 70 h (Figure 5). The IGW data can also be fitted to two different linear relationships with slightly weaker statistic performance compared with the exponential fit (Table 2). The biphasic kinetic behavior of photobleaching seen in the present study has also been observed previously and attributed to the presence of two CDOM components with differing bleaching turnover times (Del Vecchio and Blough, 2002; Grebel et al., 2009). The photobleaching of CDOM^{IGW} was apparently faster relative to that of CDOM^{BGW} (Figure 5), which could be due partly to the much stronger self-shading in BGW (Figure 9).
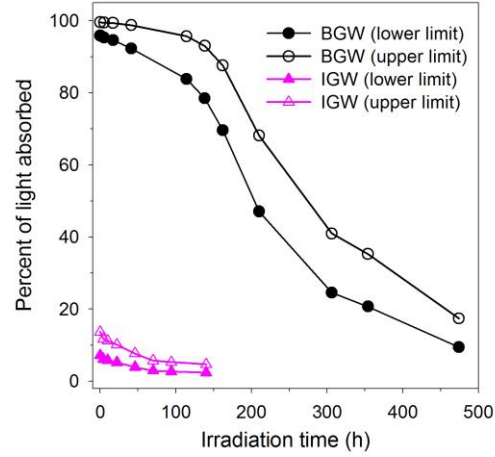
Figure 9. Percent of light absorbed by CDOM averaged over the wavelength range from 280 nm to 400 nm for time-course irradiations described in section 2.3 of the main text. The percent of light absorbed (PLA) is calculated as:

$$\text{PLA}(\lambda) = a_{\text{CDOM}}(\lambda)(a_{\text{tot}}(\lambda))^{-1}(1 - \exp(-a_{\text{tot}}(\lambda)l))$$

where l (m) denotes the pathlength of the irradiation tube, $a_{\text{CDOM}}(\lambda)$ (m^{-1}) the absorption coefficient of CDOM, and $a_{tot}(\lambda)$ (m^{-1}) the sum of $a_{CDOM}(\lambda)$ and the absorption coefficient of pure water at taken from Pope and Fry (1997) and Buiteveld et al. (1994). l is estimated using the equation of Vähätalo and Zepp (2005):

$$l = z(\mu(\lambda))^{-1}$$

where $z = 0.5\pi r$ with r being the inner radius of the irradiation tube (0.011 m) (Vähätalo and Zepp, 2005) and $\mu(\lambda)$ denotes the mean cosine of photons (dimensionless). z is estimated to be 0.0173 m for IGW (tube fully filled with sample water) and 0.0121 m for BGW (tube partially filled with sample water, see section 2.3 in the main text). The lower and upper limits of $\mu(\lambda)$ are 0.5 and 1 (Vähätalo and Zepp, 2005), giving the upper and lower limits of l and PLA, respectively. The lower and upper limits of l are 0.0121 m and 0.0242 m for BGW and 0.0173 m and 0.0346 m for IGW.
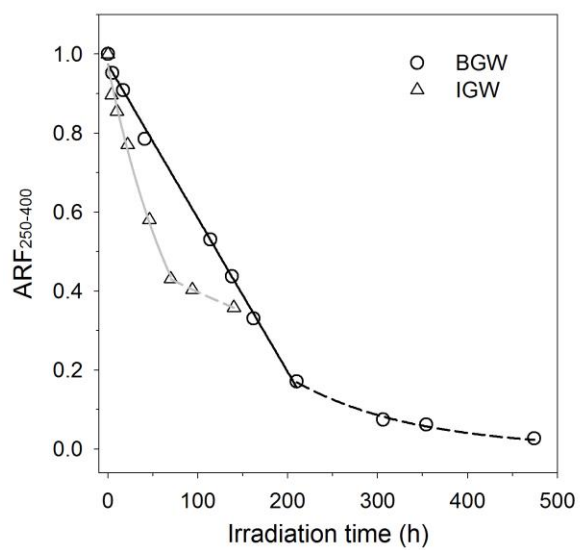
Figure 10. Average remaining fraction of CDOM absorption coefficient from 250 nm to 400 nm ($ARF_{250-400}$) *vs.* irradiation time. Lines represent best fits of the data. See Appendix for fitted equations and statistics.

3.2.3 Absorption-based indicators

Because of different extents of self-shading experienced by BGW and IGW, we chose plots of property *vs.* $ARF_{250-400}$ (except NH_4^+, see section 3.5) instead of exposure time or cumulative irradiance, to discuss the time-course data and compare the photochemical behavior of the two samples. Besides, in light of the much larger difference in E_2/E_3 than in $S_{275-295}$ between the two samples prior to irradiation (Table 3), we opted for E_2/E_3 to track the change of the spectral shape of a_{CDOM}, though results from the two parameters are similar (data not shown).

E_2/E_3 increased while $SUV\alpha_{254}$, M_W, and ρ decreased with photobleaching (Figure 11), in line with previous studies (Lou and Xie, 2006; Brooks et al., 2007). Owing partly to the more extensive bleaching of BGW, the overall changes of these parameters were far larger in BGW than in IGW, being 442% *vs.* 37.5% for E_2/E_3, 87.7% *vs.* 45.0% for $SUV\alpha_{254}$, 38.2% *vs.* 4.5% for M_W, and 27.0% vs. 2.7% for ρ. The changes of E_2/E_3 and $SUV\alpha_{254}$ for the two samples were, however, similar at comparable fractional absorption loss values (Figure 6A,B), suggesting that aromatic moieties were the dominant bleachable chromophores in both BGW and IGW. Unlike E_2/E_3 and $SUV\alpha_{254}$, the fractional losses of M_W and ρ, following linear patterns, underwent six times faster in BGW than in IGW on a relative absorption loss basis (Figure 6C). Hence, a much larger proportion of chromophores on $CDOM^{BGW}$ than on $CDOM^{IGW}$ was photochemically converted into less or non-absorbing lower-MW compounds (e.g., low-MW organic acids and inorganic carbon). This led to a substantial reduction of both the average MW and heterogeneity (i.e. smaller ρ) of $CDOM^{BGW}$, while the changes of these two quantities were marginal for $CDOM^{IGW}$.
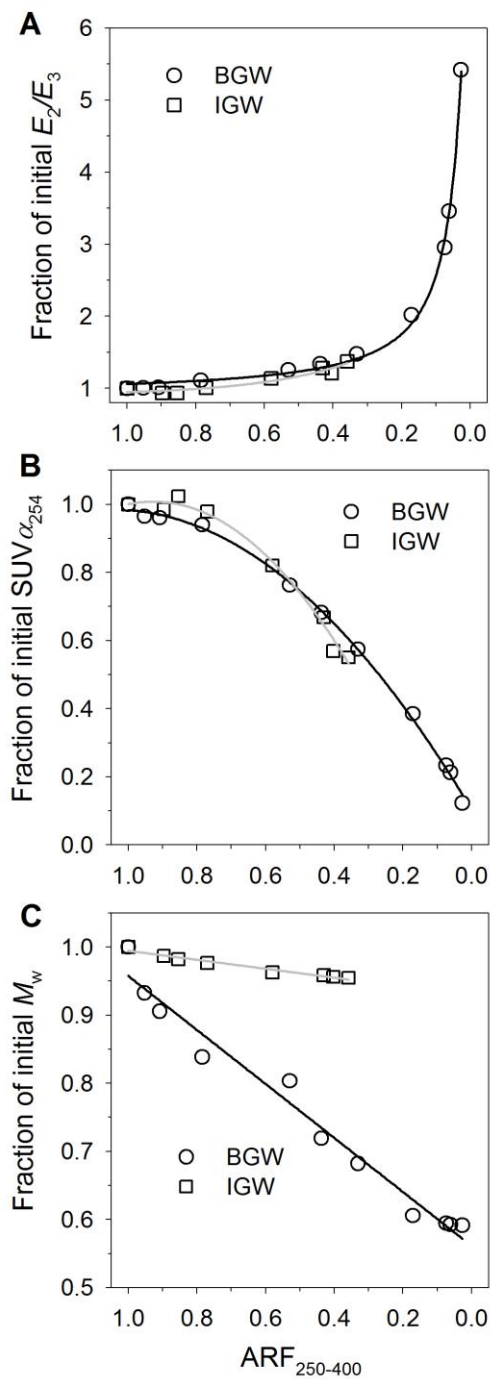
Figure 11. Fractions of initial absorption ratio E_2/E_3 (A), specific UV absorption coefficient at 254 nm (B), and weight-averaged molecular weight (C) *vs.* average remaining fraction of CDOM absorption coefficient from 250 nm to 400 nm ($ARF_{250-400}$). Black lines are best fits to BGW data and grey lines to IGW data. See Appendix for fitted equations and statistics.

3.2.3 AQYs of absorbance photobleaching

Fitted parameters for modeling the AQY spectra of absorbance photobleaching are shown in Table 5. The AQY spectra of BGW and IGW differed markedly in magnitude and shape, with $\Phi_{\mathrm{CDOM}}(\lambda)^{\mathrm{BGW}}$ superior over $\Phi_{\mathrm{CDOM}}(\lambda)^{\mathrm{IGW}}$ at $\lambda < 462$ nm but inferior to the latter at $\lambda > 462$ nm (Figure 12A). The spectrum of IGW was much flatter than that of BGW in the UV-A and visible regimes (Figure 12A). $\Phi(330)_{\mathrm{CDOM}}$ and $\overline{\Phi}_{\mathrm{CDOM}}$ for BGW were nearly 29 and eight times larger, respectively, than those of IGW (Table 5). The action spectra of the two samples both reached maxima at ~330 nm but IGW exhibited a far stronger tailing over the longer wavelengths (Figure 12B), consistent with its flatter AQY spectrum. The visible (400-600 nm) contributed 63% of the total area under the action spectrum for IGW but only 8% for BGW, demonstrating that photobleaching of IGW was dominated by the visible, whereas that of BGW by the UV.

The AQY and action spectra for IGW resemble those for the Mackenzie River water (Osburn et al. 2009) and $\overline{\Phi}_{\mathrm{CDOM}}$ for IGW is close to that for the Mackenzie River water (1.12×10^{-2} *vs*. 1.36×10^{-2}) as well (Figure 12), despite the use of different models for describing the shape of the AQY spectrum (i.e. quasi-exponential in this study vs. simple exponential by Osburn et al. (2009)). Interestingly, $\mathrm{SUV}\alpha_{254}$ for IGW (2.85 L^{-1} mg^{-1} m^{-1}) is also comparable to that for the Mackenzie River water (2.97 L^{-1} mg^{-1} m^{-1}) which was estimated from $a_{\mathrm{CDOM}}(330)$ (10.22 m^{-1}), S (18.62 $\mathrm{\mu m}^{-1}$), and DOC (512 $\mathrm{\mu mol}$ L^{-1}) reported by Osburn et al. (2009). Likewise, the higher $\overline{\Phi}_{\mathrm{CDOM}}^{\mathrm{BGW}}$ parallels its higher $\mathrm{SUV}\alpha_{25}$ (Table 1). Such a co-variation between $\overline{\Phi}_{\mathrm{CDOM}}$ and $\mathrm{SUV}\alpha_{254}$ conforms to previous observations showing a high susceptibility of phenols and other aromatic

moieties to photooxidation and similar loss rates of the aromatic components and absorbance (Sharpless and Blough, 2016 and references therein). It also complies with the positive relationships between AQY of carbon monoxide photoproduction and $SUV\alpha_{254}$ determined for CDOM in natural waters (Zhang et al., 2006; Stubbins et al., 2008) and for model aromatics (Stubbins et al., 2008). Apart from the rich aromaticity, the extraordinarily elevated Fe concentration in BGW might also have contributed to its higher efficiency of photobleaching, since Fe-mediated photo-Fenton reactions, which produce the highly oxidizing hydroxyl radical (Zepp et al., 1992), accelerate CDOM photooxidation and photobleaching (Gao and Zepp, 1998; White et al., 2003; Molot et al., 2005).

Table 5.

Fitted parameters for Eq. 2 in the text, the apparent quantum yield at 330 nm *($\Phi(330)$)*, and the solar spectrum-weighted mean apparent quantum yield ($\bar{\Phi}$) (Eq. 4 in the text) for photobleaching (m^{-1} CDOM (mol photons)$^{-1}$) and photoammonification (mol NH_4^+ (mol photons)$^{-1}$). nRMSE and R^2 are normalized root-mean-square error and coefficient of determination, respectively, for the regression of modeled against measured rates.

	Sample	m_1	m_2	m_3	$\Phi(330)$	$\bar{\Phi}$	nRMSE [a] (%)	R^2
Photobleaching	BGW	1.56×10^{-8}	6154.8	1.39	1.81	9.33×10^{-2}	8.2	0.988
	IGW	2.53×10^{-3}	280.1	-243.0	0.063	1.12×10^{-2}	6.2	0.978
Photoammonification	BGW	5.63×10^{-10}	2031.6	-165.5	1.30×10^{-4}	6.97×10^{-6}	5.4	0.997
	IGW	2.67×10^{-7}	882.6	-197.9	2.13×10^{-4}	1.69×10^{-5}	6.7	0.993
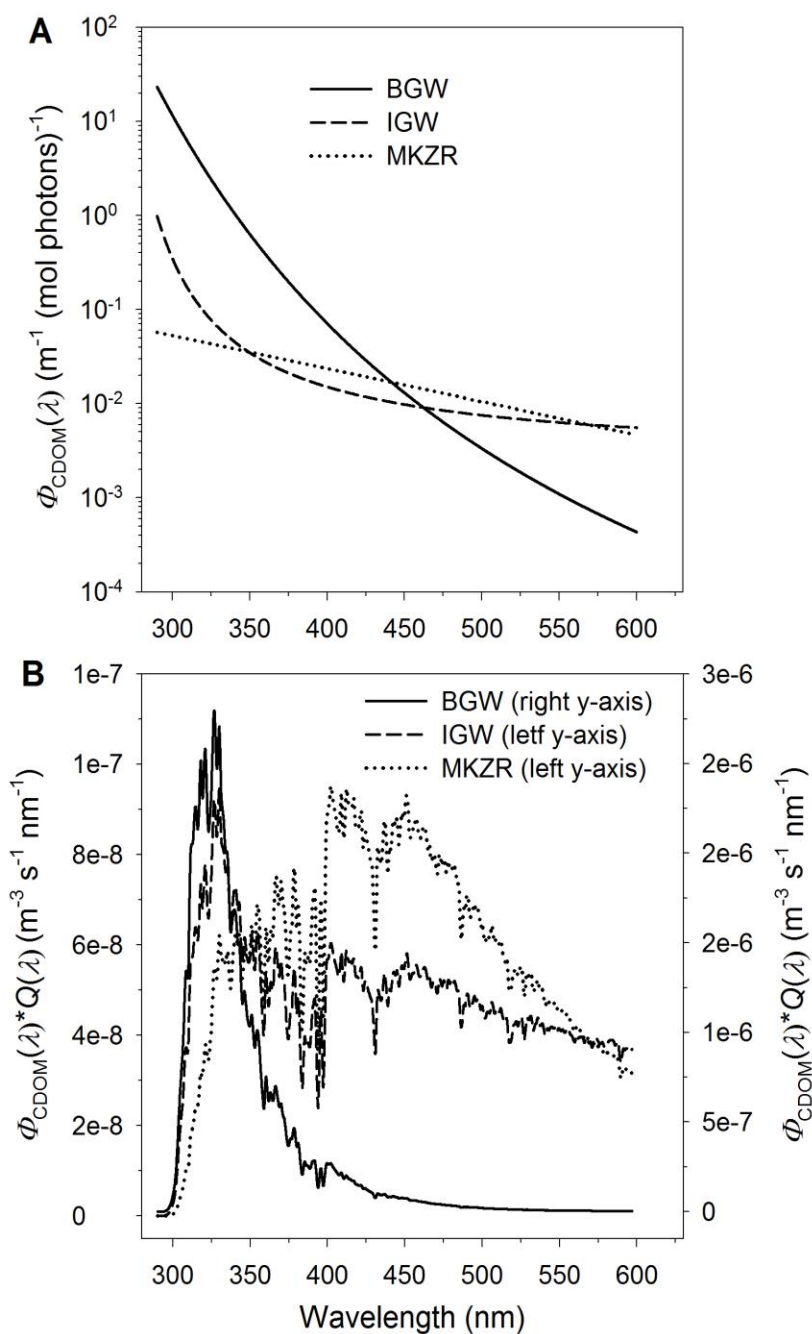
Figure 12. Apparent quantum yield (AQY) spectra of CDOM absorbance photobleaching (A) and their corresponding action spectra (B). The AQY data for the Mackenzie River (MKZR) refers to station R2 (salinity 0.1) in the study of Osburn et al. (2009).

3.3.   Photobleaching of fluorescence

3.1.7.   Fluorescence indices

For IGW, FI and HIX decreased exponentially and BIX increased linearly with photobleaching by 12.5%, 80.4%, and 30.8%, respectively, over the entire exposure period (Figure 13). BGW exhibited an overall decrease in FI (1.2%) and HIX (75.6%) and increase in BIX (30.1%) but the trends were less regular (Figure 13). For instance, the upsurge of FI^{BGW} (3.7%) over the final 1.3% absorption loss deviated from the earlier linear declining tendency (Figure 13A); BIX^{BGW} slightly fluctuated nearby the initial value before rapidly rising at $ARF_{250-400} < 0.17$ (Figure 13B); the general exponential decay of HIX^{BGW} was superimposed with a plateau over $ARF_{250-400}$ from 0.44 to 0.17. The causes underlying these irregularities are unclear. Notably, the fractional changes of all three indices $vs.$ $AFL_{250-400}$ were usually much larger in IGW than in BGW, indicating that the indices for IGW were more sensitive to photobleaching than those for BGW.

The reliance of the fluorescence indices on irradiation history seen in the present study corroborates earlier studies showing light-induced decreases in FI of riverine and wetland DOM (Brooks et al., 2006) and decreases in HIX and increases in BIX of DOM isolated from deep-ocean water (Helms et al., 2013). Hence, use of these indices for DOM source identification (FIX and BIX) and age assessment (HIX) can be imprecise or even misleading, if the targeted samples have been subjected to extensive light exposure. Under this circumstance, a larger number of compositionally based optical properties, alongside more sophisticated statistic tools, are needed to infer the source material of DOM (Hansen et al., 2016).
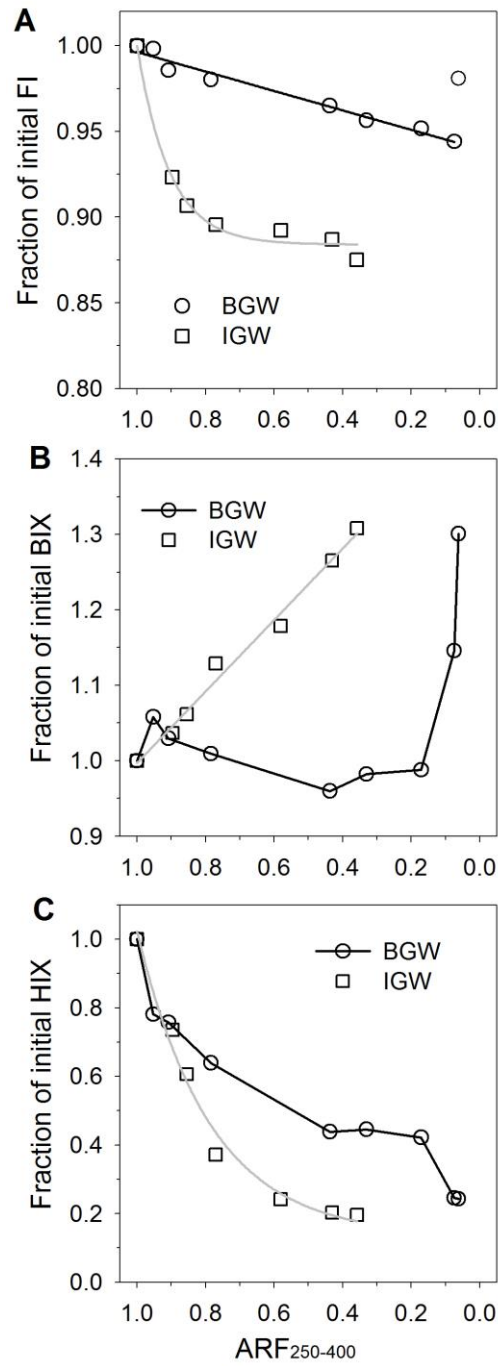
Figure 13. Fractions of initial FIX (A), BIX (B), and HIX (C) *vs.* average remaining fraction of CDOM absorption coefficient from 250 nm to 400 nm. Black line in panel A is best fit to BGW data (excluding last point) and black lines in panels B and C are data point connecting lines for BGW. Grey lines in panel A-C are best fits to IGW data. See Appendix for fitted equations and statistics.

3.1.8. EMM peaks and PARAFAC components

After full-length irradiations, the intensities of peak A dropped by 79% for BGW and 72% for IGW, and peak C by 73% and 68%, respectively. The large decreases in the intensities of these peaks demonstrate a rapid photodegradation of humic-like material, which is consistent with the results of earlier studies (Helms et al., 2013; Timko et al., 2015) and with the photochemical losses of $SUV\alpha_{254}$ and MW (section 3.2). The ratio of peak C to A, an indication of the amount of humic acid-like *vs.* fulvic acid-like fluorophores (Chen et al., 2003; Hansen et al., 2016), increased from 0.79 to 1.01 for BGW and from 0.66 to 0.78 for IGW, suggesting a preferential photodegradation of fulvic acids like FDOM. Notably, the originally vague fluorescence signals adjoining the lower edge of peak A^{IGW} (Figure 3B) became a distinct peak centered at $\lambda_{ex}/\lambda_{em}$ 255 nm/356 nm (peak X herein) after irradiation (Figure 3D). The appearance of peak X was due more likely to the decay of peak A than to an increase of its intensity or the formation of a new peak, since the fluorescence signal at $\lambda_{ex}/\lambda_{em}$ 255 nm/356 nm diminished during the first 22 h irradiation ($0.240 \rightarrow 0.209$ R.U.) and thereafter remained rather constant (0.207 ± 0.0025 R.U.). The initial decline of this fluorescence signal apparently arose from the dwindling of peak A's periphery which likely masked peak X at the beginning (Figure 3B). Peak X falls into the broad protein-like category defined by Chen et al. (2003), suggesting that this proteinaceous material is photochemically recalcitrant. Previous studies also reported photochemical resistance of protein-like fluorescence peaks (Cory et al., 2007; Clark et al., 2008). In terms of the EEM location, peak X is blue-shifted by 20 nm in excitation and red-shifted by 16 nm in emission relative to peak

T (protein- and tryptophan-like) defined by Coble (2007) (Table 1 and Figure 3B). The blue shift in excitation implies that the protein-like material signified by peak X may possess a higher aromaticity than the protein- or tryptophan-like material denoted by peak T.

Figure 14 shows F_{max} of PARAFAC components as a function of $ARF_{250-400}$. For BGW, C1 decayed gently up to $ARF_{250-400}$ ~0.2 and then abruptly with further bleaching (Figure 14A). The overall decay trends of C2, C3, and C4 encountered minor to moderate rebounds during the late stage of photobleaching (Figure 14B-D); the causes underlying these bulges are unclear. C5 remained undetectable up to $ARF_{250-400}$ 0.44 when it started rising rapidly (Figure 14E), contrasting with the behavior of C1-C4. C1 to C4 declined by 62%, 89%, 87%, and 64%, respectively, at the end of irradiation, thereby enhancing the relative abundances of C1 and C4 but diminishing those of C2 and C3 (Figure 15). For IGW, all components decreased with photobleaching, exponentially for C1 and linearly for C2-C5. C1–C5 dropped by 100%, 80%, 84%, 73%, and 38%, respectively, after the entire exposure period, which greatly increased the relative abundance of C4 among the humic components (C1-C4) (Figure 15). The fractional loss of C1 in IGW underwent much faster than that in BGW (Figure 14A), while the differences in the loss of C2–C4 between the two samples were considerably smaller (Figure 14B-D). After full-length irradiations, BGW was further enriched with C1 relative to IGW due to the complete disappearance of C1 in IGW (Figure 15).

The loss of the PARAFAC humic components (C1-C4) is consistent with the reduced intensities of the humic-like EEM peaks A and C. The behavior of C1-C4 further reveals that 1) both the terrestrial (C1-C2) and the autochthonous (C3-C4) humic-like

52

components are photochemically reactive; 2) the photolabilities of C2-C4 are comparable on both intra- and inter-sample bases; 3) the photolability of C1 in IGW is much higher than that of C1 in BGW (and also higher than any other components in both samples), pointing to C1 being the dominant UV absorber in IGW, the presence of different subclasses of C1 in BGW and IGW and/or different matrix effects on photodegradation of C1. The loss of the protein-like C5 in IGW is inconsistent with the constancy of the intensity of its protein-like EEM peak X, suggesting that C5 and peak X may represent different classes of proteinaceous compounds that vary in photolability. Similarly, Bittar et al. (2015) suspected that peak T may comprise multiple protein constituents that differ in composition and hence photolability. The formation of C5 in BGW implies the photochemical synthesis of protein-like or related nitrogen-containing structures. Cory et al. (2015) also observed that solar irradiation increased the fluorescence intensity of protein-like FDOM in stream water. Nitrogen-containing organic compounds or moieties (e.g. amine, amide, amino acids) can be produced from photochemical transformation of CDOM (Bushaw et al., 1996; Tarr et al., 2001) or photochemical incorporation of inorganic nitrogen (nitrate, nitrite, and ammonium) into DOM (Kieber et al., 1997; Thorn and Cox, 2012).
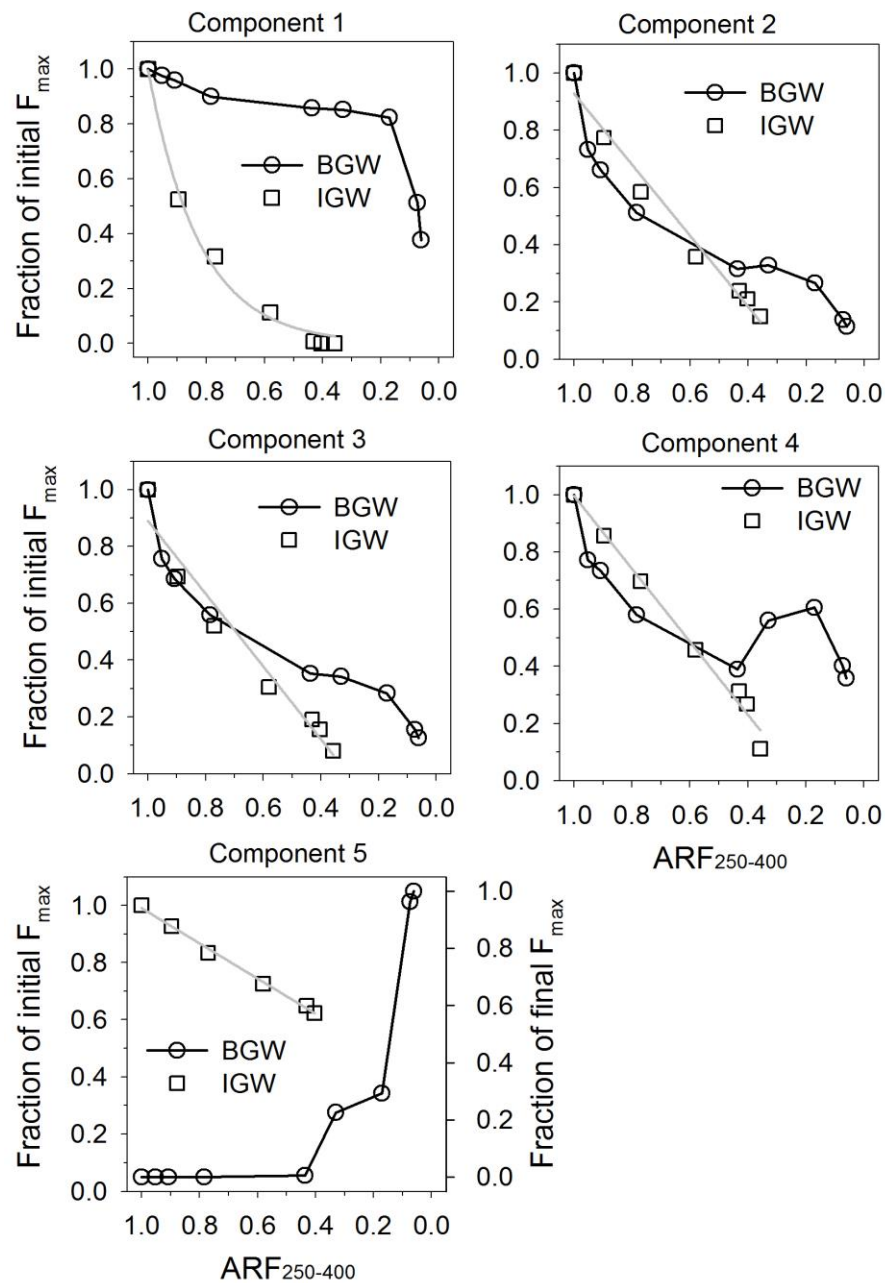
Figure 14. Fractions of initial or final maximum fluorescence intensities of five PARAFAC-modeled components *vs.* average remaining fraction of CDOM absorption coefficient from 250 nm to 400 nm. In panel E, the right y-axis is for BGW and the left for IGW. The final absolute F_{max} value for BGW is 1.72 R.U. Black lines are data point connecting lines for BGW. Grey lines are best fits to IGW data. See Appendix for fitted equations and statistics.
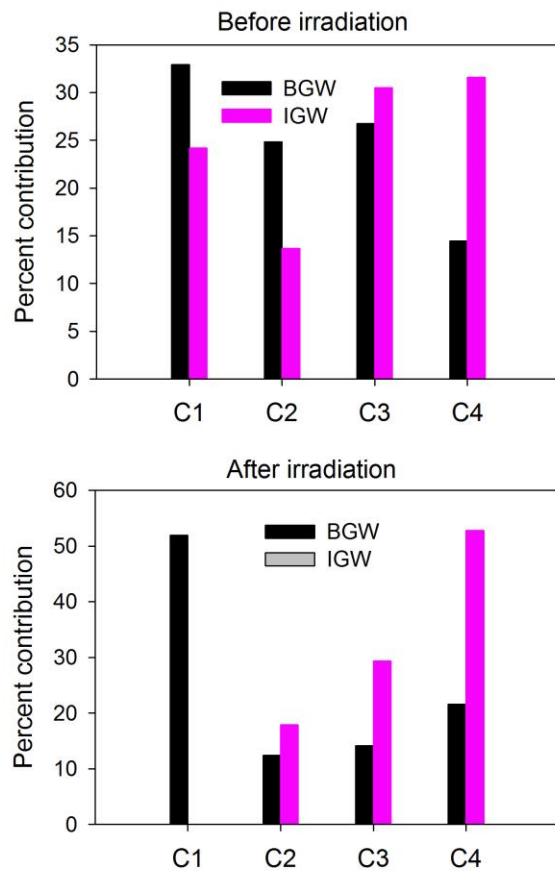
Figure 15. Percent contribution of each individual component among C1-C4 to the summation of C1-C4 before and after full-length irradiations (i.e. 474 h for BGW and 140 h for IGW). The percent contribution of component i is defined as $F_{\max(i)}\Big/\sum_{i=1}^{4} F_{\max(i)} \times 100$, where $F_{\max(i)}$ is the maximum fluorescence intensity of component i.

3.4. DOC photomineralization

Throughout the exposure periods, the fractional losses of DOC were consistently lower than those of absorption coefficient for both BGW and IGW (Figure 16A). The ratio of DOC loss to $AFL_{250-400}$ ($R_{DOC/CDOM}$) remained nearly constant, 0.33 for BGW and 0.19 for IGW over much of the photobleaching regimes ($AFL_{250-400}^{BGW} \leq 0.83$ and $AFL_{250-400}^{IGW} \leq 0.57$) (Figure 16B) but increased with further bleaching (Figure 16A). $R_{DOC/CDOM}^{BGW}$ was close to that for the Saguenay River surface water (0.36; Zhang and Xie, 2015), which is also highly colored with a $SUV\alpha_{254}$ of 4.78 L mg^{-1} m^{-1} comparable to $SUV\alpha_{254}^{BGW}$ (5.39 L m^{-1} mg^{-1}). The lower $R_{DOC/CDOM}^{IGW}$ suggests a larger portion of DOM^{IGW} being colorless or absorbing weakly, consistent with its lower $SUV\alpha_{254}$, and/or a higher fraction of the photolyzed chromophores on $CDOM^{IGW}$ being converted to colorless or weakly-absorbing DOM instead of DIC, congruent with the smaller decreases in MW and polydispersity of $CDOM^{IGW}$ described in section 3.1.1.

AQYs of photochemical DOC losses (Φ_{DOC}) for BGW could not be derived from the time-series irradiation, because the irradiation tubes containing BGW were partially filled with air (section 2.3), which made it difficult to quantify the photons absorbed in these tubes. On the other hand, as DOC was not measured due to technical constraints during the multispectral irradiations using cutoff filters, Φ_{DOC} could not be directly obtained from these experiments, either. However, given the similarity in the spectral compositions of the radiation under the WG280 cutoff filter and the full-spectrum radiation used in the time-series exposures (Figure 17), the DOC losses under WG280 can be estimated by the corresponding $AFL_{250-400}$ multiplied by $R_{DOC/CDOM}$ obtained from the time-series irradiations. Note that the $AFL_{250-400}$ under WG280 (BGW: 0.063; IGW:

0.10) were within the $AFL_{250-400}$ ranges showing linear relationships between the fractional DOC loss and $AFL_{250-400}$ (Figure 16B). The number of photons absorbed by CDOM was calculated using Eq. 1. and integrated from 290 nm to 450 nm. The choice of this wavelength range for integration is based on two factors: 1) photomineralization is driven predominantly by the UV radiation (Powers and Miller, 2015) and 2) the light source used in the present study exhibited multiple irradiance spikes between 450 nm and 500 nm (Figure 17) which would underestimate Φ_{DOC}^{BGW} relative to Φ_{DOC}^{IGW}, since the absorption spectrum of BGW was flatter and far more elevated across the visible regime than that of IGW (Figure 2). Dividing the moles of DOC loss by the moles of photons absorbed gives a broadband Φ_{DOC} over the 280-450 nm wavelength range. The Φ_{DOC} (mol DOC (mol photons)$^{-1}$) thus obtained was 1.42×10^{-3} for BGW and 6.98×10^{-4} for IGW, the former being a factor of two of the latter.

The higher photomineralization efficiency of BGW could be linked to its stronger aromaticity, as inferred from the positive correlation between DIC photoproduction AQY and $SUV\alpha_{254}$ in freshwater lakes (Koehler et al., 2016). However, the twofold difference in Φ_{DOC} between BGW and IGW is much smaller than their eightfold disparity in $\overline{\Phi}_{CDOM}$ (section 3.2.3), suggesting that aromaticity is less important in controlling photomineralization than photobleaching. Photodecarboxylation has been identified as a major mechanism for DOM photomineralization (Ward and Cory, 2016). Interestingly, preferential photodecarboxylation occurs with the highly oxidized, weaker UV-absorbing aliphatic carboxylic acids rather than the less oxidized and strong UV-absorbing aromatic acids (Ward and Cory, 2016). Our result is thus consistent with the finding of Ward and Cory (2016). Similar to photobleaching, the very rich Fe content in BGW would also

enhance its photomineralization efficiency through the reaction of DOM with hydroxyl radicals generated from the photo-Fenton reactions (Gao and Zepp, 1998; Goldstone et al., 2002), even though this effect could be lessened due to the relatively weak acidity (pH: 6.29, Table 3) of the sample (Gu et al., 2017).
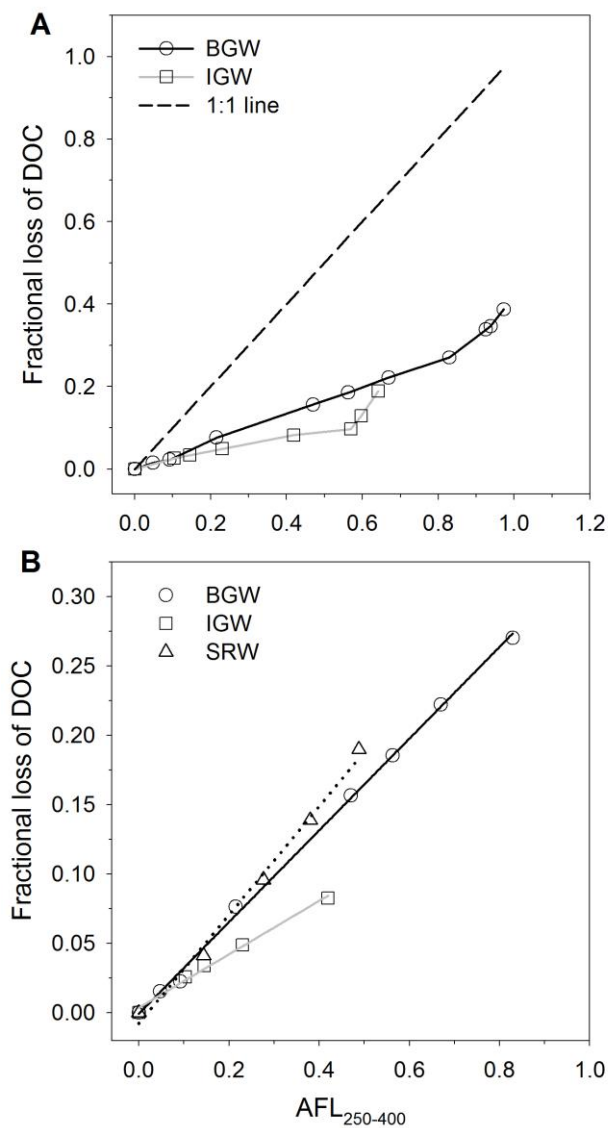
Figure 16. Fractional loss of DOC *vs.* average fractional loss of CDOM absorption coefficient from 250 nm to 400 nm for all data points (A) and excluding the last three data points (B). Lines in panel B are best fits to data (see Appendix for fitted equations and statistics). For comparison, the Saguenay River water (SRW) data is included (Zhang and Xie, 2015).
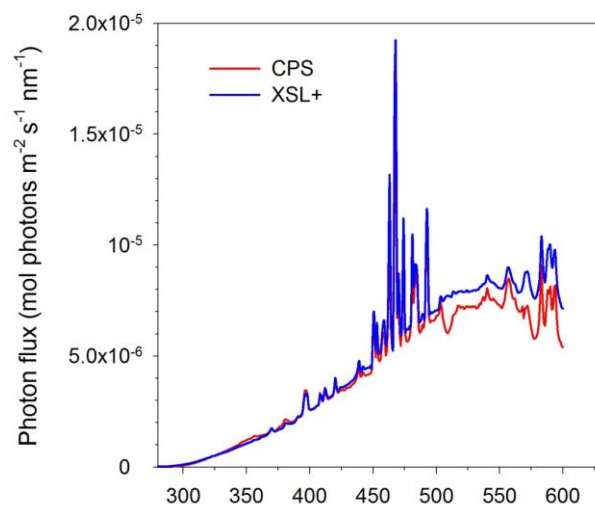
Figure 17. Photon flux spectra of the SUNTES CPS (under cutoff filter WG280) and XLS+ (without cutoff filters) solar simulators. The CPS was used for AQY experiments and the XLS+ for time-course irradiations described in Chapter 2.

3.4.1. Photoammonification

Results from the time-series irradiations are shown with plots of NH_4^+ concentration

vs. absolute loss of absorption coefficient averaged over 250-400 nm (Δa_{CDOM}(250-400))

(Figure 18). NH_4^+ concentration increased linearly with photobleaching at Δa_{CDOM}(250-

400)^{BGW}< 87.56 m^{-1} (R^2 = 0.985) and Δa_{CDOM}(250-400)^{IGW}< 1.73 m^{-1} (R^2 = 0.975) and

leveled off with further bleaching. Over the linear ranges, the amount of NH_4^+ produced

per unit of Δa_{CDOM}(250-400) in IGW (1.12 μmol L^{-1} m) was 80 times higher than in

BGW (0.014 μmol L^{-1} m), demonstrating that DOM^{IGW} was highly enriched relative to

DOM^{BGW} with reactive NH_4^+ precursors and/or sensitizers mediating

photoammonification, if secondary photoprocesses were involved. An enrichment of

NH_4^+ precursors on DOM^{IGW} is in accordance with the detection of the protein-like EEM

peak X and PARAFAC C5 in IGW and their absence in BGW (section 3.1.3). The

decreases in the NH_4^+ production rate suggest a depletion of the precursors and/or the

photosensitizers. Alternatively, it could arise from an increased incorporation of NH_4^+

into DOM at higher NH_4^+ concentrations (Thorn and Mikita, 1992; Kieber et al., 1997;

Gardner et al., 1998; Koopmans and Bronk, 2002; Kitidis et al., 2008; Thorn and Cox,

2012). Declining photoammonification rates with increasing photobleaching have also

been reported for humic extract solutions and coastal and oligotrophic waters (Bushaw et

al., 1996; Vähätalo and Zepp, 2005; (Kitidis et al. 2006).

Fitted parameters for modeling the AQY spectra of photoammonification are shown

in Table 5. The two samples displayed similar $\Phi_{NH_4^+}$ values in the UVB regime but

$\Phi_{NH_4^+}{}^{IGW}$ became increasingly larger than $\Phi_{NH_4^+}{}^{BGW}$ with increasing wavelength over the

UVA and visible bands (Figure 19A). The $\Phi_{NH_4^+}$ values obtained by the present study are comparable to those reported for a low-salinity Baltic Sea water sample (Stedmon et al., 2007) but substantially higher than those determined with the Mackenzie River water (Xie et al., 2012) (Figure 19A). In terms of $\Phi_{NH_4^+}(330)$ and $\overline{\Phi}_{NH_4^+}$, IGW exceeded BGW by 63.8% and 140%, respectively (Table 5), starkly contrasting with the much lower $\overline{\Phi}_{CDOM}^{IGW}$ $vs.$ $\overline{\Phi}_{CDOM}^{BGW}$. $\overline{\Phi}_{NH_4^+}$ for IGW is two orders of magnitude higher than that for the Mackenzie River water (1.4×10^{-7}) and 54% higher than that for the coastal Baltic Sea sample (1.1×10^{-5}), revealing large variability of the photoammonification efficiency in natural waters. UV (mainly UV-A) dominated the action spectra of both IGW and BGW while the contribution of the visible band was considerably higher in IGW (32%) than in BGW (6%) (Figure 19B) due to the AQY spectrum of IGW being flatter at longer wavelengths (Figure 19A). The visible contribution in IGW is close to that in the Baltic Sea sample (25%) but significantly lower than that for the Mackenzie River water (51%).

The higher $\Phi_{NH_4^+}^{IGW}$ over $\Phi_{NH_4^+}^{BGW}$ indicates that neither aromaticity nor Fe concentration is the dominant determinant on the photoammonification efficiency. Xie et al. (2012) observed a seaward increase in $\Phi_{NH_4^+}$ from the inshore Mackenzie River estuary towards the offshore Canada Basin and Arnos et al. (2012) reported increasing $\Phi_{NH_4^+}$ with increasing salinity in the Baltic Sea. As low-salinity waters contain more aromatic carbon-rich DOM and often more dissolved Fe as well, the results from these two studies are consistent with those from the present study. Xie et al. (2012) further revealed that $\Phi_{NH_4^+}$ co-varies with the ratio of dissolved organic nitrogen (DON) to DOC (the data of Arnos et al. (2012) manifested the same trend, though these authors did not

explicitly discuss this issue), implying that the concentration of NH_4^+ precursors relative to that of DOC is an important control on $\Phi_{NH_4^+}$. Since DOM^{IGW} was likely enriched with NH_4^+ precursors compared with DOM^{BGW} (see discussion above in this section), the higher $\Phi_{NH_4^+}{}^{IGW}$ is in keeping with the earlier finding.

3.4.2. Photochemical turnover of groundwater DOM in the receiving water body

To a first approximation, the photochemical turnover time of a constituent of groundwater DOM (τ_{DOM}, d) in the receiving water body can be estimated as:

$$\tau_{DOM} = [DOM]N^{-1}\left(\Phi_{DOM}\int_{290}^{600} a_{CDOM}(\lambda)(a_{TOT}(\lambda))^{-1}Z^{-1}N^{-1}Q_{d0-}(\lambda)d\lambda\right)^{-1}$$

$$= Z[DOM]\Phi_{DOM}^{-1}\left(\int_{290}^{600} a_{CDOM}(\lambda)(a_{TOT}(\lambda))^{-1}Q_{d0-}(\lambda)d\lambda\right)^{-1} \qquad (6)$$

where τ_{DOM} stands for the photochemical turnover time of CDOM absorbance (τ_{CDOM}), DOC (τ_{DOC}) or DON (τ_{DON}); [DOM] for the concentration of CDOM (represented by $a_{CDOM}(330)$), DOC (mol m^{-3}) or DON (mol m^{-3}) in groundwater; Φ_{DOM} for $\overline{\Phi}_{CDOM}$, the broadband Φ_{DOC} (section 3.4), or $\overline{\Phi}_{NH_4^+}$; N for the dilution factor due to mixing with the receiving water; Z for the surface mixed layer or photoactive layer depth (m), whichever is deeper; $a_{TOT}(\lambda)$ for the total absorption coefficient (m^{-1}) in the receiving water, i.e. the sum of the absorption coefficients of CDOM, suspended particles, and water; $Q_{d0-}(\lambda)$ for the downwelling solar photon flux just below the water surface (mol photons m^{-2} d^{-1} nm^{-1}). Z, $a_{TOT}(\lambda)$, and $Q_{d0-}(\lambda)$ are common terms for both BGW and IGW.

The ratio of $a_{CDOM}(330)^{BGW}/a_{CDOM}(330)^{IGW}$ is ~89, $\bar{\Phi}_{CDOM}^{BGW}/\bar{\Phi}_{CDOM}^{IGW}$ ~8, and $a_{CDOM}(\lambda)^{BGW}/a_{CDOM}(\lambda)^{IGW}$ ranges from 69 at 290 nm to 330 at 600 nm and averages 173. Eq. 6 thus indicates that τ_{CDOM}^{BGW} is at least six times shorter than τ_{CDOM}^{IGW} (69*8/89 = 6.2). The ratio of DOC^{BGW}/DOC^{IGW} is 31 and $\Phi_{DOC}^{BGW}/\Phi_{DOC}^{IGW}$ ~2, thereby leading to τ_{DOC}^{BGW} being at least four times shorter than τ_{DOC}^{IGW} (69*2/31 = 4.4). Estimating the ratio of $\tau_{DON}^{BGW}/\tau_{DON}^{IGW}$ poses potentially higher uncertainties, since the exact ratio of DON^{BGW}/DON^{IGW} is unknown. However, an upper limit of DON^{BGW}/DON^{IGW} can be derived by equating it to DOC^{BGW}/DOC^{IGW} (i.e. 31), considering that DOM^{BGW} is depleted with protein-like components relative to DOM^{IGW} (section 3.1.3). Assuming NH_4^+ to be the dominant inorganic nitrogen photoproduct from DON (Mopper et al., 2015) and using the known values of $\bar{\Phi}_{NH_4^+}^{BGW}/\bar{\Phi}_{NH_4^+}^{IGW}$ (0.71) and $a_{CDOM}(\lambda)^{BGW}/a_{CDOM}(\lambda)^{IGW}$ ($\geq$69), the upper limit of $\tau_{DON}^{BGW}/\tau_{DON}^{IGW}$ is estimated to be 0.32 (i.e. 31*0.71/69). The photochemical turnover of DON^{BGW} with respect to photoammonification is thus more than three times faster than that of DON^{IGW}. Likewise, BGW is a bigger photochemical source of NH_4^+ than IGW, despite $\Phi_{NH_4^+}^{IGW}$ being higher than $\Phi_{NH_4^+}^{BGW}$.

This preliminary assessment demonstrates that the photochemical turnovers of CDOM absorbance, DOC, and DON for DOM^{BGW} are all substantially quicker than those for DOM^{BGW} due partly (photobleaching and photomineralization) or entirely (photoammonification) to the very large ratio of $a_{CDOM}(\lambda)^{BGW}/a_{CDOM}(\lambda)^{IGW}$ making DOM^{BGW} the dominant photon absorber. A key assumption underlying this assessment is that the change in DOM photoreactivity during seaward transport is small compared with the difference in the original photoreactivity between the two DOM pools or that their

photoreactivities are affected to similar extents. Transport-derived photoreactivity alterations may arise from biogeochemical processes occurring in the aquifers and from mixing of groundwater with seawater. Given the narrow discharge zone and the short groundwater residence time in the sampling area (section 2.1.), the biogeochemical effect may be limited. Increases in salinity and pH during physical mixing may also alter the DOM photoreactivity but few relevant data are available in the literature. Reported effects of salinity on CDOM photobleaching in surface freshwater range from negligible (Song et al., 2016) to ~10% (Minor et al., 2006) and are ~30-40% on DOC photomineralization (Minor et al., 2006). These values are small relative to the differences in CDOM absorption and AQYs of photobleaching and photomineralization between BGW and IGW. Effects of salinity and pH on photoammonification are unknown.
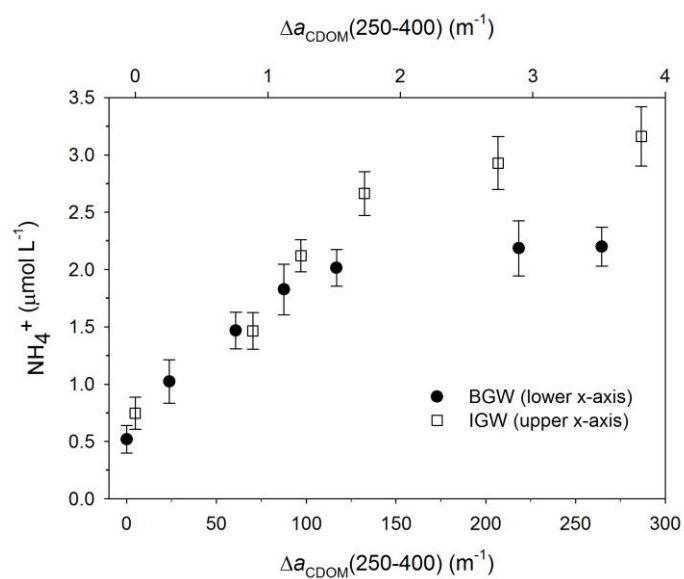
Figure 18. Ammonium concentration vs. loss of absorption coefficient averaged over 250-400 nm during time-course irradiations. Error bars represent absolute differences of duplicate samples.
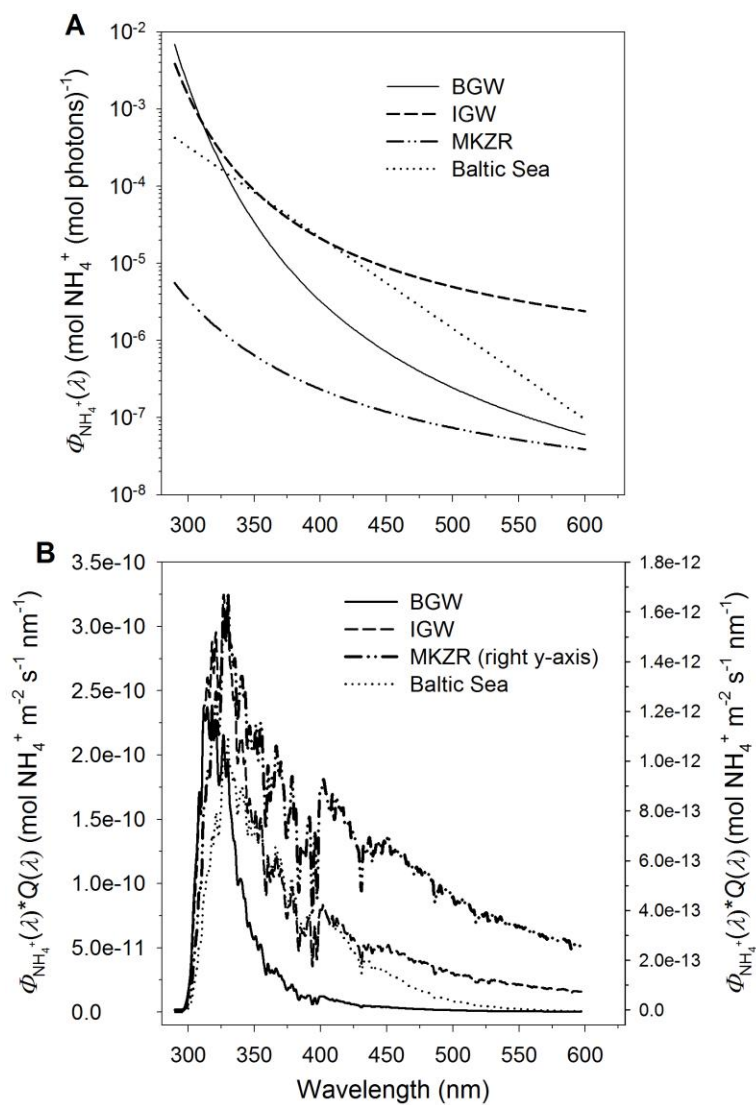
Figure 19. Apparent quantum yield spectra of ammonium photoproduction (A) and their corresponding action spectra (B). For comparison, data from Xie et al. (2012, station 697, salinity 0.15) and Stedmon et al. (2007, station Arkona, salinity 7.7), are included.

Chapter 4. Conclusions

This study assessed the photoreactivities of two groundwater DOM pools with contrasting chemical and optical properties. Absorption and fluorescence spectroscopy revealed that BGW predominantly comprised strongly colored, old, high-MW DOM of terrestrial origin while IGW was largely composed of less colored, fresh, low-MW DOM of microbial origin. For both BGW and IGW, exposure to solar-simulated radiation led to increases in E_2/E_3, BIX, and NH_4^+ and decreases in DOC, MW, absorbance, $SUV\alpha_{254}$, FI, HIX, humic-like EEM peaks A and C, and humic-like PARAFAC C1-C4. On a fractional-absorption-loss basis, the photochemically induced fractional changes in BGW were comparable to those in IGB for $SUV\alpha_{245,}$ E_2/E_3, and C2-C4, considerably larger for MW, BIX, and DOC, and substantially smaller for FIX, HIX, and C1. On an absorbed-photon basis, DOM^{BGW} was far more, moderately more, and less photoreactive than DOM^{IGW} in terms of absorbance photobleaching, DOC photomineralization, and photoammonification, respectively. The differing AQYs of these three major photoprocesses conform to the distinct chemical compositions of the two DOM pools elucidated by the spectroscopy. Photochemical turnovers of CDOM absorption, DOC, and DON in the receiving water body is likely much faster for DOM^{BGW} than for DOM^{IGW} due to the much higher UV and visible absorption of DOM^{BGW}.

As DOM in groundwater experiences little prior light exposure, our results are instrumental for characterizing photoreactivities of different organic source materials in natural waters, particularly those of terrigenous and microbial origins. Generalization of the findings from the present study and those reported previously for surface waters leads to a tentative paradigm: terrigenous DOM is more prone to absorbance photobleaching

but less prone to photoammonification than microbial-derived DOM while the two DOM pools are comparably reactive with respect to DOC photomineralization. The mechanisms behind this pattern are poorly understood and warrant further investigations. Note that this paradigm is based on AQYs not the absolute rates of the photoprocesses in question. In freshwater systems (except large lakes), estuaries, and coastal zones strongly impacted by river runoff, terrestrial CDOM is usually the dominant absorber of the photochemistry-driving UV and visible radiation. In these aquatic environments, the rate of NH_4^+ photoproduction from terrigenous DOM can be higher than that from autochthonous DOM of microbial origin despite the lower AQY for the former.

Conclusions

Cette étude a évalué les photoréactivités de deux échantillons DOM d'un aquifère présentant des propriétés chimiques et optiques contrastées. Les spectroscopies d'absorption et de fluorescence ont révélé que la DOM BGW comprenait principalement des composés d'origine terrestre fortement colorés, anciens et de haut poids MW tandis que la DOM IGW était en grande partie composé de matière d'origine microbienne moins colorée, plus fraîche et de faible MW. Pour BGW et IGW, l'exposition au rayonnement solaire simulé a entraîné des augmentations de E2/E3, de l'indice BIX et de la concentration en NH_4^+ et des diminutions de la teneur en DOC, des MW, de l'absorbance, du $SUV\alpha254$, des indices FI et HIX, des intensités des pics A et C des matrices d'excitation-émission de fluorescence et des constituants PARAFAC C1-C4, de type humique. Sur la base de la perte relative d'absorption, suite à l'irradiation, les changements photochimiques induits dans BGW étaient comparables à ceux dans IGB pour $SUV\alpha245$, E2/E3 et les constituants PARAFAC C2-C4. De plus, ils étaient considérablement plus grands pour MW, BIX et DOC et sensiblement plus petits pour FIX, HIX et le constituant PARAFAC C1. Sur la base de photons absorbés, DOM BGW était beaucoup plus, modérément plus et moins photoréactif que DOM IGW en termes de photoblanchiment de l'absorbance, de photominéralisation du DOC et de la photoammonification, respectivement. Les différents rendements quantiques apparents, AQY, de ces trois photoprocédés majeurs sont conformes aux compositions chimiques distinctes des deux pools DOM élucidés par la spectroscopie. Les temps de transformation photochimique de l'absorption de la matière organique colorée, CDOM, du DOC et de l'azote organique dissous, DON, dans les eaux côtières sont

vraisemblablement beaucoup plus rapides pour DOM BGW que pour DOM IGW. Cela est en grande partie ou entièrement en raison de l'absorption, dans l'UV et le visible, beaucoup plus importante pour DOM BGW. La présence d'un paléosol (la principale source présumée de DOM BGW dans cette étude) sur la côte est de l'Amérique du Nord (Grant, 1970; Gehrels, 1994) et l'enfouissement prévu des aquifères côtiers actuels en raison de l'élévation du niveau de la mer (Post al., 2013) appellent à davantage d'études sur les impacts biogéochimiques potentiels de la décharge des eaux souterraines (submarine groundwater discharge, SGD), y compris ceux qui résultent de la photochimie des DOM, dans les eaux côtières. Comme les eaux souterraines contenant les DOM sont généralement peu exposées à la lumière, nos résultats sont essentiels pour caractériser les photoréactivités de différentes matières organiques dans les eaux naturelles, en particulier celles d'origines terrigène et microbienne. La généralisation des résultats de la présente étude, combiné à ceux rapportés précédemment pour les eaux de surface, conduit à un paradigme provisoire: le DOM terrigène est plus sujet au photoblanchiment de l'absorbance mais moins sujet à la photoammonification que la DOM d'origine microbienne tandis que les deux DOM présentent une réactivité comparable pour la photominéralisation du DOC. Les mécanismes sous-jacents à ce modèle sont mal compris et justifient des recherches plus approfondies. Notez que ce paradigme est basé sur les AQY et non sur les taux absolus des photoprocédés en question. Dans les systèmes d'eau douce (sauf les grands lacs), les estuaires et les zones côtières fortement touchés par le ruissellement des rivières, le CDOM terrestre est habituellement l'absorbeur dominant du rayonnement ultraviolet menant à des transformations photochimiques. Dans ces milieux aquatiques, le taux de photoproduction de NH_4^+ des DOM terrigènes peut être supérieur

à celui des DOM autochtones d'origine microbienne, malgré l'AQY plus faible pour les premiers.

Bibliography

Aarnos, H., Ylöstalo, P., Vähätalo, A.V., 2012. Seasonal phototransformation of dissolved organic matter to ammonium, dissolved inorganic carbon, and labile substrates supporting bacterial biomass across the Baltic Sea. Journal of Geophysical Research 117, G01004. doi:10.1029/2010JG001633.

Aiken, G., 2014. Fluorescence and dissolved organic matter: a chemist's perspective. In: Aquatic organic matter fluorescence, Coble, P.G., Lead, J., Baker, A., Reynolds, D.M., Spencer, R.G.M. (eds). Cambridge University Press, New York, New York, USA, pp. 35-74.

Andrews, S. S., Caron, S., Zafiriou. O.C., 2000. Photochemical oxygen consumption in marine waters: A major sink for colored dissolved organic matter? Limnology and Oceanography 45, 267-277.

Anschutz, P., Smith, T., Mouret, A., Deborde, J., Bujan, S., Poirier, D., Lecroart, P., 2009. Tidal sands as biogeochemical reactors. Estuarine, Coastal and Shelf Science 84, 84–90.

Baker, M.A., Valett, H.M., Dahm, C.N., 2000. Organic carbon supply and metabolism in a shallow groundwater ecosystem. Ecology 81, 3133–3148.

Babin, M., Stramski, D., Ferrari, G. M., Claustre, H., Bricaud, A., Obolensky, G., Hoepffner, N., 2003. Variations in the light absorption coefficients of phytoplankton, nonalgal particles, and dissolved organic matter in coastal waters around Europe. Journal of Geophysical Research 108, 3211, doi:10.1029/2001JC000882.

Beck, A.J., Tsukamoto, Y., Tovar-Sanchez, A., Huerta-Diaz, M., Bokuniewicz, H.J., Sañudo-Wilhelmy, S. A., 2007. Importance of geochemical transformations in determining submarine groundwater discharge-derived trace metal and nutrient fluxes. Applied Geochemistry 22, 477–490.

Bertilsson, S., Stepanauskas, R., Cuadros-Hansson, R., Graneli, W., Wikner, J., Tranvik, L., 1999. Photochemically induced changes in bioavailable carbon and nitrogen pools in a boreal watershed. Aquatic Microbial Ecology 19, 47–56.

Birdwell, J.E., Engel, A.S., 2010. Characterization of dissolved organic matter in cave and spring waters using UV–Vis absorbance and fluorescence spectroscopy. Organic Geochemistry 41, 270–280.

Bittar, T.B., Vieira, A.A., Stubbins, A., Mopper, K., 2015. Competition between photochemical and biological degradation of dissolved organic matter from the cyanobacteria Microcystis aeruginosa. Limnology and Oceanography 60, 1172-1194.

Blough, N.V., Zepp, R.G., 1995. Reactive oxygen species in natural waters, in: Foote, C.S., Valentine, J., Greenberg, A., Liebman, J.F. (Eds.), Active Oxygen in Chemistry. Springer, Berlin Heidelberg, pp. 280–333.

Blough, N.V., Del Vecchio, R., 2002. Chromophoric DOM in the coastal environment. In: Biogeochemistry of Marine Dissolved Organic Matter, Hansell, D.A., Carlson, C.A. (eds), Academic Press, New York, New York, USA, pp. 509-546.

Boehme, J., Coble, P., Conmy, R., Stovall-Leonard, A., 2004. Examining CDOM fluorescence variability using principal component analysis: seasonal and regional

modeling of three-dimensional fluorescence in the Gulf of Mexico. Marine Chemistry 89, 3–14.

Brisebois, D., 1981. Lithostratigraphie des strates permo-carboniferes, de l'archipel des Iles de la Madeleine. Ministère de l'énergie et des ressources. Direction des communications. Québec, Québec, pp. 48.

Bro, R., 1997. PARAFAC. Tutorial and applications. Chemometrics and Intelligent Laboratory Systems 38, 149–171.

Brooks, M.L., Meyer, J.S., McKnight, D.M., 2006. Photooxidation of wetland and riverine dissolved organic matter: altered copper complexation and organic composition. Hydrobiologia 579, 95–113.

Brooks, M.L., McKnight, D. M., Clements, W.H., 2007. Photochemical control of copper complexation by dissolved organic matter in Rocky Mountain streams, Colorado. Limnology and Oceanography, 52, 766-779.

Buiteveld, H., Hakvoort, J.H.M., Donze, M., 1994. Optical properties of pure water. Proceedings of SPIE 2258, Ocean Optics XII, 174–183.

Burnett, W.C., Bokuniewicz, H., Huettel, M., Moore, W.S., Taniguchi, M., 2003. Groundwater and pore water inputs to the coastal zone. Biogeochemistry 66, 3–33.

Burnett, W.C., Taniguchi, M., Oberdorfer, J., 2001. Measurement and significance of the direct discharge of groundwater into the coastal zone. Journal of Sea Research 46, 109–116.

Bushaw, K.L., Zepp, R.G., Tarr, M.A., Schultz-Jander, D., Bourbonniere, R.A., Hodson, R.E., Miller, W.L., Bronk, D.A., Moran, M.A., 1996. Photochemical release of

biologically available nitrogen from aquatic dissolved organic matter, Nature 381, 404–407.

Cai, W.-J., Wang, Y., Krest, J., Moore, W.S., 2003. The geochemistry of dissolved inorganic carbon in a surficial groundwater aquifer in North Inlet, South Carolina, and the carbon fluxes to the coastal ocean. Geochimica et Cosmochimica Acta 67, 631–639.

Chaillou, G., Couturier, M., Tommi-Morin, G., Rao, A.M.F., 2014. Total Alkalinity and Dissolved Inorganic Carbon Production in Groundwaters Discharging through a Sandy Beach. Procedia Earth and Planetary Science 10, 88 – 99.

Chaillou, G., Lemay-Borduas, F., Couturier, M., 2015. Transport and transformations of groundwater-borne carbon discharging through a sandy beach to a coastal ocean. Canadian Water Resources Journal 41, 455-468.

Chen, W., Westerhoff, P., Leenheer, J.A., Booksh, K., 2003. Fluorescence excitation−emission matrix regional integration to quantify spectra for dissolved organic matter. Environmental Science and Technology 37, 5701-5710.

Chin, Y.-P., Aiken, G., O'Loughlin, E., 1994. Molecular Weight, Polydispersity, and Spectroscopic Properties of Aquatic Humic Substances. Environmental Science and Technology 28, 1853–1858.

Clark, C.D., Litz, P.L., Grant, S.B, 2008. Salt marshes as a source of chromophoric dissolved organic matter (CDOM) to southern California coastal waters. Limnology and Oceanography 53, 1923-1933.

Coble, P.G., 1996. Characterization of marine and terrestrial DOM in seawater using excitation-emission matrix spectroscopy. Marine Chemistry 51, 325–346.

Coble, P.G., 2007. Marine optical biogeochemistry: the chemistry of ocean color. Chemical reviews 107, 402-418.

Cory, R.M., 2005. Redox and Photochemical Reactivity of Dissolved Organic Matter in Surface Waters. PhD thesis, University of Colorado, Boulder, CO, 252.

Cory, R.M., Mcneill, K., Cotner, J.P., Amado, A., Purcell, J.M., Marshall, A.G., 2010. Singlet oxygen in the coupled photochemical and biochemical oxidation of dissolved organic matter. Environmental Science and Technology 44, 3683–3689.

Cory, R.M., Harrold, K.H., Neilson, B.T., Kling, G.W., 2015. Controls on dissolved organic matter (DOM) degradation in a headwater stream: the influence of photochemical and hydrological conditions in determining light-limitation or substrate-limitation of photo-degradation. Biogeosciences12, 6669-6685.

Cory, R.M., McKnight, D.M., Chin, Y.-P., Miller, P., Jaros, C.L., 2007. Chemical characteristics of fulvic acids from Arctic surface waters: Microbial contributions and photochemical transformations. Journal of Geophysical Research: Biogeosciences 112, doi:10.1029/2006JG000343.

Couturier, M., Nozais, C., Chaillou, G., 2016. Microtidal subterranean estuaries as a source of fresh terrestrial dissolved organic matter to the coastal ocean. Marine Chemistry 186, 46-57.

Couturier, M., Tommi-Morin, G., Sirois, M., Rao, A., Nozais, C., Chaillou, G., 2017. Nitrogen transformations along a shallow subterranean estuary. Biogeosciences 14, 3321.

Deflandre, B., Mucci, A., Gagné, J.P., Guignard, C., Sundby, B., 2002. Early diagenetic processes in coastal marine sediments disturbed by a catastrophic sedimentation event. Geochimica et Cosmochimica Acta 66, 2547-2558.

Del Vecchio, R., Blough N. V., 2002. Photobleaching of chromophoric dissolved organic matter in natural waters: kinetics and modeling. Marine Chemistry 78, 231-253.

Doane, T.A., Horwáth, W.R., 2010. Eliminating interference from iron(III) for ultraviolet absorbance measurements of dissolved organic matter. Chemosphere 78, 1409−1415.

Fichot, C.G., Benner, R., 2012. The spectral slope coefficient of chromophoric dissolved organic matter (S275-295) as a tracer of terrigenous dissolved organic carbon in river-influenced ocean margins. Limnology and Oceanography 57, 1453-1466.

Faust, B.C., Zepp, R.G., 1993. Photochemistry of aqueous iron(III)-polycarboxylate complexes: roles in the chemistry of atmospheric and surface waters. Environmental Science and Technology 27, 2517–2522.

Gao, H., Zepp, R.G., 1998. Factors influencing photoreactions of dissolved organic matter in a coastal river of the southeastern United States. Environmental Science and Technology 32, 2940-2946.

Gardner, W.S., Cavaletto, J.F., Bootsma, H.A., Lavrentyev, P.J., Troncone, F., 1998. Nitrogen cycling rates and light effects in tropical Lake Maracaibo. Venezuela. Limnology and Oceanography 43, 1814–1825.

Goñi, M.A., Gardner, I.R., 2003. Seasonal dynamics in dissolved organic carbon concentrations in a coastal water-table aquifer at the forest-marsh interface. Aquatic Geochemistry 9, 209–232.

Grant, D.R., 1970. Recent coastal submergence of the Maritime Provinces, Canada. Canadian Journal of Earth Sciences 7, 676–89.

Grebel, J.E., Pignatello, J.J., Song, W., Cooper, W.J., Mitch, W.A., 2009. Impact of halides on the photobleaching of dissolved organic matter. Marine Chemistry 115, 134-144.

Gu, Y., Lensu, A., Perämäki, S., Ojala, A., Vähätalo, A.V., 2017. Iron and pH regulating the photochemical mineralization of dissolved organic carbon. ACS Omega 2, 1905-1914.

Hansen, A.M., Kraus, T.E., Pellerin, B.A., Fleck, J.A., Downing, B.D., Bergamaschi, B.A., 2016. Optical properties of dissolved organic matter (DOM): Effects of biological and photolytic degradation. Limnology and Oceanography 61, 1015-1032.

Helms, J.R., Mao, J., Schmidt-Rohr, K., Abdulla, H., Mopper, K., 2013. Photochemical flocculation of terrestrial dissolved organic matter and iron. Geochimica et Cosmochimica Acta 121, 398–413.

Helms, J. R., Stubbins, A., Perdue, E. M., Green, N. W., Chen, H., Mopper, K., 2013. Photochemical bleaching of oceanic dissolved organic matter and its effect on absorption spectral slope and fluorescence. Marine Chemistry155, 81-91.

Helms, J.R., Mao, J., Stubbins, A., Schmidt-Rohr, K., Spencer, R.G.M., Hernes, P.J., Mopper, K., 2014. Loss of optical and molecular indicators of terrigenous dissolved organic matter during long-term photobleaching. Aquatic Sciences 76, 353–373.

Helms, J.R., Stubbins, A., Ritchie, J.D., Minor, E.C., Kieber, D.J., Mopper, K., 2008. Absorption spectral slopes and slope ratios as indicators of molecular weight, source, and photobleaching of chromophoric dissolved organic matter. Limnology and Oceanography 53, 955–969.

Holmes, R.M., Aminot, A., Kérouel, R., Hooker, B.A., and Peterson, B.J., 1999. A simple and precise method for measuring ammonium in marine and freshwater ecosystems. Canadian Journal of Fisheries and Aquatic Sciences 56, 1801–1808.

Hong, J., Xie, H., Guo, L., Song, G., 2014. Carbon monoxide photoproduction: Implications for photoreactivity of Arctic permafrost-derived soil dissolved organic matter. Environmental Science and Technology 48, 9113−9121.

Hu, C., Muller-Karger, F.E., Zepp, R.G., 2002. Absorbance, absorption coefficient, and apparent quantum yield: A comment on common ambiguity in the use of these optical concepts. Limnology and Oceanography 47, 1261–1267.

Huguet, A., Vacher, L., Relexans, S., Saubusse, S., Froidefond, J.M., Parlanti, E., 2009. Properties of fluorescent dissolved organic matter in the Gironde Estuary. Organic Geochemistry 40, 706–719.

Johannessen, S.C., Miller, W.L., 2001. Quantum yield for the photochemical production of dissolved inorganic carbon in seawater. Marine Chemistry 76, 271–283.

Johannesson, K.H., Chevis, D.A., Burdige, D.J., Cable, J.E., Martin, J.B., Roy, M., 2011. Submarine groundwater discharge is an important net source of light and middle REEs to coastal waters of the Indian River Lagoon, Florida, USA. Geochimica Cosmochimica Acta 75, 825–843.

Johnson, W.P., Bao, G., John, W.W., 2002. Specific UV Absorbance of Aldrich Humic Acid: Changes during Transport in Aquifer Sediment. Environmental Science and Technology 36, 608–616.

Juneau M-N. Hausse récente du niveau marin relatif aux îles de la Madeleine: Mémoire de maîtrise, Université du Québec à Rimouski; 2012;151 p.

Kieber, R.J., Dydro, L.H., Seaton, P.J., 1997. Photooxidation of triglycerides and fatty acids in seawater: implication toward the formation of marine humic substances. Limnology and Oceanography 42, 1454–1462.

Kitidis, V., Uher, G., Upstill-Goddard, R.C., Mantoura, R.F.C., Spyres, G., Woodward, E.M.S., 2006. Photochemical production of ammonium in the oligotrophic Cyprus Gyre (Eastern Mediterranean). Biogeosciences 3, 439–449.

Kitidis, V., Uher, G., Woodward, E.M.S., Owens, N.J.P., Upstill-Goddard, R.C., 2008. Photochemical production and consumption of ammonium in a temperate river–sea system. Marine Chemsitry 112, 118–127.

Koehler, B., Broman, E., Tranvik, L.J., 2016. Apparent quantum yield of photochemical dissolved organic carbon mineralization in lakes. Limnology and Oceanography 61, 2207-2221.

Koopmans, D.J., Bronk, D.A., 2002. Photochemical production of dissolved inorganic nitrogen and primary amines from dissolved organic nitrogen in waters of two estuaries and adjacent surficial groundwaters. Aquatic Microbial Ecology 26, 295–304.

Lawaetz, A.J., Stedmon, C.A., 2009. Fluorescence Intensity Calibration Using the Raman Scatter Peak of Water. Applied Spectroscopy 63, 936–940.

Loiselle, S. A., Bracchini, L., Dattilo, A.M., Ricci, M., Tognazzi, A., Cózar, A., Rossi, C., 2009. The optical characterization of chromophoric dissolved organic matter using wavelength distribution of absorption spectral slopes. Limnology and Oceanography 54, 590-597.

Lou, T., Xie, H., 2006. Photochemical alteration of the molecular weight of dissolved organic matter. Chemosphere 65, 2333–2342.

Mack, J., Bolton, J.R., 1999. Photochemistry of nitrite and nitrate in aqueous solution: a review. Journal of Photochemistry and Photobiology A: Chemistry 128, 1-13.

McKnight, D.M., Boyer, E.W., Westerhoff, P.K., Doran, P.T., Kulbe, T., Andersen, D.T., 2001. Spectrofluorometric characterization of dissolved organic matter for indication of precursor organic material and aromaticity. Limnology and Oceanography 46, 38–48.

Miller, W.L., Zepp, R.G., 1995. Photochemical production of dissolved inorganic carbon from terrestrial organic matter: Significance to the oceanic organic carbon cycle. Geophysical Research Letters 22, 417–420.

Miller, W.L., 1998. Effects of UV radiation on aquatic humus: Photochemical principles and experimental considerations. In: Aquatic humic substances-Ecology and biogeochemistry, Hessen, D.O., Tranvik, L.J. (eds), Springer, Berlin Heidelberg, Germany, pp. 125-143.

Molot, L.A., Hudson, J.J., Dillon, P.J., Miller, S.A., 2005. Effect of pH on photo-oxidation of dissolved organic carbon by hydroxyl radicals in a coloured, softwater stream. Aquatic Sciences-Research Across Boundaries 67, 189-195.

Moore, W.S., 2010. The effect of submarine groundwater discharge on the ocean. Annual Review of Marine Science 2, 59–88.

Mopper, K., Kieber, D.J., Stubbins, A., 2015. Marine photochemistry of organic matter: processes and impacts. In: Biogeochemistry of Marine Dissolved Organic Matter, Hansell, D.A., Carlson, C.A. (eds). Academic Press, San Diego, California, USA, pp. 389−450.

Nelson, N.B., Siegel, D.A., 2013. The global distribution and dynamics of chromophoric dissolved organic matter. Annual Review of Marine Science 5, 447-476.

Ohno, T., 2002. Fluorescence Inner-Filtering Correction for Determining the Humification Index of Dissolved Organic Matter. Environmental Science and Technology 36, 742–746.

Ohno, T., Chorover, J., Omoike, A., Hunt, J., 2007. Molecular weight and humification index as predictors of adsorption for plant- and manure-derived dissolved organic matter to goethite. European Journal of Soil Science 58, 125–132.

Osburn, C.L., Morris, D.P., 2003. Photochemistry of chromophoric dissolved organic matter in natural waters. In: UV Effects in Aquatic Organisms and Ecosystems, Helbling, E.W., Zagarese, H. (eds.).The Royal Society of Chemistry, Cambridge, UK, pp. 185-217.

Osburn, C.L., Retamal, L., Vincent, W.F., 2009a. Photoreactivity of chromophoric dissolved organic matter transported by the Mackenzie River to the Beaufort Sea. Marine Chemistry 115, 10–20.

Osburn, C.L., O'Sullivan, D.W., Boyd, T.J., 2009b. Increases in the longwave photobleaching of chromophoric dissolved organic matter in coastal waters. Limnology and Oceanography 54, 145-159.

Peuravuori, J., Pihlaja, K., 1997. Molecular size distribution and spectroscopic properties of aquatic humic substances. Analytica Chimica Acta 337, 133-149.

Pope, R.M., Fry, E.S., 1997. Absorption spectrum (380-700 nm) of pure water. II. Integrating cavity measurements. Applied Optics 36, 8710–8723.

Porcal, P., Dillon, P.J., Molot, L.A., 2014. Interaction of extrinsic chemical factors affecting photodegradation of dissolved organic matter in aquatic ecosystems. Photochemical and Photobiological Sciences 13, 799-812.

Poulin, B.A., Ryan, J.N., Aiken, G.R., 2014. Effects of iron on optical properties of dissolved organic matter. Environmental Science and Technology 48, 10098-10106.

Powers, L.C., Miller, W.L., 2015. Hydrogen peroxide and superoxide photoproduction in diverse marine waters: A simple proxy for estimating direct CO2 photochemical fluxes. Geophysical Research Letters 42, 7696-7704.

Powers, L.C., Miller, W.L., 2015. Photochemical production of CO and CO2 in the Northern Gulf of Mexico: Estimates and challenges for quantifying the impact of photochemistry on carbon cycles. Marine Chemistry 171, 21-35.

Santos, I.R., Burnett, W.C., Dittmar, T., Suryaputra, I.G.N.A., Chanton, J., 2009. Tidal pumping drives nutrient and dissolved organic matter dynamics in a Gulf of Mexico subterranean estuary. Geochimica et Cosmochimica Acta 73, 1325–1339.

Sazawa, K., Tachi, M., Wakimoto, T., Kawakami, T., Hata, N., Taguchi, S., Kuramitz, H., 2011. The evaluation for alterations of DOM components from upstream to downstream flow of rivers in Toyama (Japan) using three-dimensional excitation-emission matrix fluorescence spectroscopy. International Journal of Environmental Research and Public Health 8, 1655–1670.

Scott, D.B., Brown, K., Collins, E.S., Medioli, F.S., 1995. A new sea-level curve from Nova Scotia: Evidence for a rapid acceleration of sea-level rise in the late mid-Holocene. Canadian Journal of Earth Sciences 32, 2071–80.

Sharpless, C.M., Blough, N.V., 2014. The importance of charge-transfer interactions in determining chromophoric dissolved organic matter (CDOM) optical and photochemical properties. Environmental Science: Processes & Impacts 16, 654-671.

Sharpless, C.M., Aeschbacher, M., Page, S.E., Wenk, J., Sander, M., McNeill, K., 2014. Photooxidation-induced changes in optical, electrochemical, and photochemical

properties of humic substances. Environmental Science and Technology 48, 2688–2696.

Shen, Y., Chapelle, F.H., Strom, E.W., Benner, R., 2015. Origins and bioavailability of dissolved organic matter in groundwater. Biogeochemistry 122, 61-78.

Slomp, C.P., Van Cappellen, P., 2004. Nutrient inputs to the coastal ocean through submarine groundwater discharge: controls and potential impact. Journal of Hydrology 295, 64–86.

Song, G., Xie, H., Bélanger, S., Leymarie, E., Babin, M., 2013. Spectrally resolved efficiencies of carbon monoxide (CO) photoproduction in the western Canadian Arctic: Particles versus solutes. Biogeosciences 10, 3731-3748.

Spencer, R.G.M., Stubbins, A., Hernes, P.J., Baker, A., Mopper, K., Aufdenkampe, A.K., Dyda, R.Y., Mwamba, V.L., Mangangu, A.M., Wabakanghanzi, J.N., Six, J., 2009. Photochemical degradation of dissolved organic matter and dissolved lignin phenols from the Congo River. Journal of Geophysical Research 114, G03010, doi:10.1029/2009JG000968.

Stedmon, C.A., Bro, R., 2008. Characterizing dissolved organic matter fluorescence with parallel factor analysis: a tutorial. Limnology and Oceanography: Methods 6, 572–579.

Stedmon, C.A., Markager, S., 2003. Behaviour of the optical properties of coloured dissolved organic matter under conservative mixing. Estuarine, Coastal and Shelf Science 57, 973–979.

Stedmon, C.A., Markager, S., Tranvik, L., Kronberg, L., Slätis, T., Martinsen, W., 2007. Photochemical production of ammonium and transformation of dissolved organic matter in the Baltic Sea. Marine Chemistry 104, 227–240.

Stedmon, C.A., Nelson, N.B., 2015. The optical properties of DOM in the Ocean. In: Biogeochemistry of Marine Dissolved Organic Matter, Hansell, D.A., Carlson, C.A. (eds). Academic Press, San Diego, California, USA, pp. 481–508.

Stedmon, C.A., Osburn, C.L., Kragh, T., 2010. Tracing water mass mixing in the Baltic–North Sea transition zone using the optical properties of coloured dissolved organic matter. Estuar. Estuarine, Coastal and Shelf Science 87, 156–162.

Stubbins, A., Hubbard, V., Uher, G., Law, C.S., Upstill-Goddard, R.C., Aiken, G.R., Mopper, K., 2008. Relating carbon monoxide photoproduction to dissolved organic matter functionality. Environmental Science and Technology 42, 3271-3276.

Tarr, M.A., Wang, W., Bianchi, T.S., Engelhaupt, E., 2001. Mechanisms of ammonia and amino acid photoproduction from aquatic humic and colloidal matter. Water Research 35, 3688–3696.

Timko, S.A., Gonsior, M., Cooper, W.J., 2015. Influence of pH on fluorescent dissolved organic matter photo-degradation. Water Research 85, 266-274.

Thorn, K.A., Mikita, M.A., 1992. Ammonia fixation by humic substances: A nitrogen-15 and carbon-13 NMR study, Science of the Total Environment 113, 67–87.

Thorn, K.A., Cox, L.G., 2012. Ultraviolet irradiation effects incorporation of nitrate and nitrite nitrogen into aquatic natural organic matter. Journal of Environmental Quality 41, 865-881.

Vähätalo, A.V., Wetzel, R.G., 2008. Long-term photochemical and microbial decomposition of wetland-derived dissolved organic matter with alteration of 13C:12C mass ratio. Limnology and Oceanography 53, 1387–1392.

Vähätalo, A.V., Wetzel, R.G., 2004. Photochemical and microbial decomposition of chromophoric dissolved organic matter during long (months–years) exposures. Marine Chemistry 89, 313–326.

Vähätalo, A.V., Zepp, R.G., 2005. Photochemical mineralization of dissolved organic nitrogen to ammonium in the Baltic Sea. Environmental Science and Technology 39, 6985–6992.

Valiela, I., Costa, J., Foreman, K., Teal, J.M., Howes, B., Aubrey, D., 1999. Transport of groundwater-borne nutrients from watersheds and their effects on coastal waters. Biogeochemistry 10, 177–197.

Ward, C.P., Cory, R.M., 2016. Complete and partial photo-oxidation of dissolved organic matter draining permafrost soils. Environmental Science and Technology 50, 3545-3553.

Weishaar, J.L., Aiken, G.R., Bergamaschi, B.A., Fram, M.S., Fujii, R., Mopper, K., 2003. Evaluation of Specific Ultraviolet Absorbance as an Indicator of the Chemical Composition and Reactivity of Dissolved Organic Carbon. Environmental Science and Technology 37, 4702–4708.

White, E.M., Kieber, D.J., Sherrard, J., Miller, W.L., Mopper, K., 2010. Carbon dioxide and carbon monoxide photoproduction quantum yields in the Delaware Estuary. Marine Chemistry 118, 11–21.

White, E.M., Vaughan, P.P., Zepp, R.G., 2003. Role of the photo-Fenton reaction in the production of hydroxyl radicals and photobleaching of colored dissolved organic matter in a coastal river of the southeastern United States. Aquatic Sciences-Research Across Boundaries 65, 402-414.

Wickland, K.P., Neff, J.C., Aiken, G.R., 2007. Dissolved organic carbon in Alaskan boreal forest: sources, chemical characteristics, and biodegradability. Ecosystems 10, 1323–1340.

Windom, H.L., Moore, W.S., Niencheski, L.F.H., Jahnke, R.A., 2006. Submarine groundwater discharge: A large, previously unrecognized source of dissolved iron to the South Atlantic Ocean. Marine Chemistry 102, 252–266.

Xiao, Y.H., Sara-Aho, T., Hartikainen, H., Vähätalo, A.V., 2013. Contribution of ferric iron to light absorption by chromophoric dissolved organic matter. Limnology and Oceanography 58, 653-662.

Xie, H., Bélanger, S., Song, G., Benner, R., Taalba, A., Blais, M., Tremblay, J.-É., Babin, M., 2012. Photoproduction of ammonium in the southeastern Beaufort Sea and its biogeochemical implications. Biogeosciences 9, 3047–3061.

Zepp, R.G., 2003. Solar UVR and aquatic carbon, nitrogen, sulfur and metals cycles. In: UV Effects in Aquatic Organisms and Ecosystems, Helbling, E.W., Zagarese, H. (eds.).The Royal Society of Chemistry, Cambridge, UK, pp. 137–184.

Zepp, R.G., Faust, B.C., Hoigné, J., 1992. Hydroxyl radical formation in aqueous reactions (pH 3-8) of iron (II) with hydrogen peroxide: the photo-Fenton reaction. Environmental Science and Technology 26, 313–319.

Zhang, Y., Xie, H., 2015. Photomineralization and photomethanification of dissolved organic matter in Saguenay River surface water. Biogeosciences 12, 6823–6836.

Zhang, Y., Xie, H., Chen, G., 2006. Factors affecting the efficiency of carbon monoxide photoproduction in the St. Lawrence Estuarine System (Canada). Environmental Science and Technology 40, 7771–7777.

Appendix

Statistics of regression analysis for figures 10, 11, 13, 14, and 16 in the main text

Figure	Sample label	Equation	a±SE	b±SE	c±SE	R^2	*p*	*n*
5	BGW (upper part)	Y=a*X+b	-0.0039±0.00008	0.97±0.01	N/A	0.997	<0.0001	8
	BGW (lower part)	Y=a*exp(-b*X)	0.82±0.13	0.0075±0.0006	N/A	0.991	0.004	4
	IGW (upper part)	Y=a*exp(-b*X)	0.97±0.02	0.011±0.001	N/A	0.990	<0.0001	6
	IGW (upper part)	Y=a*X+b	-0.0077±0.0005	0.95±0.02	N/A	0.982	0.0001	6
	IGW (lower part)	Y=a*exp(-b*X)	0.52±0.002	0.0026±0.00005	N/A	1.000	0.01	3
	IGW (lower part)	Y=a*X+b	-0.0010±0.00004	0.50±0.0045	N/A	0.998	0.03	3
6	BGW (panel A)	Y=a*exp(b/(X+c))	0.891± 0.037	0.188±0.016	0.077±0.008	0.997	<0.0001	11
	IGW (panel A)	Y=a*exp(-b*X)+c	1.66±1.07	3.69±2.16	0.91±0.09	0.929	0.001	8
	BGW (panel B)	Y=a*X+b*X^2+c	1.69±0.06	-0.81±0.05	0.10±0.01	0.998	<0.0001	11
	IGW (panel B)	Y=a*X+b*X^2+c	2.72±0.35	-1.47±0.26	-0.25±0.10	0.989	<0.0001	8
	BGW (panel C)	Y=a*X+b	0.40±0.02	0.56±0.01	N/A	0.976	<0.0001	11
	IGW (panel C)	Y=a*X+b	0.066±0.005	0.93±0.004	N/A	0.962	<0.0001	8
	BGW (panel D)	Y=a*X+b	0.265±0.013	0.714±0.008	N/A	0.979	<0.0001	11
	IGW (panel D)	Y=a*X+b	0.043±0.002	0.956±0.002	N/A	0.983	<0.0001	8
8	BGW (panel A)	Y=a*X+b	0.057±0.004	0.94±0.003	N/A	0.972	<0.0001	8
	IGW (panel A)	Y=a*exp(b*X)+c	$(3.0±4.2)*10^{-6}$	10.6±1.4	0.88±0.004	0.986	0.0002	7
	IGW (pane B)	Y=a*X+b	-0.47±0.02	1.47±0.02	N/A	0.988	<0.0001	7
	IGW (panel C)	Y=a*exp(b*X)+c	0.0082±0.0069	4.68±0.83	0.13±0.05	0.985	0.0002	7
9	IGW (panel A)	Y=a*exp(b*X)	0.0035±0.0013	5.66±0.40	N/A	0.993	<0.0001	7
	IGW (panel B)	Y=a*X+b	-0.31±0.055	1.24±0.081	N/A	0.979	<0.0001	7
	IGW (panel C)	Y=a*X+b	-0.39±0.078	1.28±0.11	N/A	0.962	0.0001	7
	IGW (panel D)	Y=a*X+b	-0.28±0.042	1.28±0.062	N/A	0.988	<0.0001	7
	IGW (panel E)	Y=a*X+b	0.37±0.014	0.62±0.019	N/A	0.996	<0.0001	7
10	BGW (panel B)	Y=a*X+b	0.33±0.005	-0.0007±0.0023	N/A	0.999	<0.0001	8
	IGW (panel B)	Y=a*X+b	0.19±0.01	0.0036±0.0022	N/A	0.992	0.0003	5
	SRW (panel B)	Y=a*X+b	0.39±0.02	-0.0076±0.0062	N/A	0.992	0.0003	5